Ore Geology Reviews 101 (2018) 293–311

Contents lists available at ScienceDirect

Ore Geology Reviews

journal homepage: www.elsevier.com/locate/oregeorev

Mineralogy of the Tumanny Au-Ag-Te-Hg epithermal veins, Western Chukchi Peninsula, Russia

Ivan A. Baksheev[a,*], Evgeny A. Vlasov[a], Yurii N. Nikolaev[a], Nadezhda N. Krivitskaya[a], Nataliya N. Koshlyakova[a], Ekaterina V. Nagornaya[a], Taras V. Kara[b], Georgy T. Dzhedzheya[a]

[a] Geology Department, Lomonosov Moscow State University, Leninskie Gory, Moscow 119991, Russia
[b] Polyus LLC, Tverskoy Blvd 13, bld 1, Moscow 123104, Russia

ARTICLE INFO

Keywords:
Epithermal
Intermediate sulfidation
Tumanny Au-Ag-Te-Hg prospect
Chukchi Peninsula
Russia

ABSTRACT

The Tumanny Au-Ag-Te-Hg epithermal prospect, Chukchi Peninsula, Russia is located in the near contact zone of the large Vuknei pluton, part of the Early Cretaceous Egdykgych Complex, which is related to the Peschanka porphyry copper deposit and the Nakhodka porphyry-epithermal ore district located 45 km north of Tumanny. Mineralization at Tumanny is characterized by an early carbonate-base metal and a late gold-silver-sulfosalt mineral assemblage. Pyrite of the first assemblage is unzoned and As-poor, and tennantite-tetrahedrite solid solutions (Ttr_s) are characterized by a weak oscillatory zoning caused by variable contents of Sb and As, low Ag content, and the widely variable Sb/(Sb + As) values. Pyrite of the second assemblage is zoned and As-rich (up to 5.2 wt%) and Ttr_s is weakly zoned and Ag-rich (up to 10.35 apfu) and has a comparatively narrow range of Sb/(Sb + As) value. Electrum, Au-Ag alloy ("küstelite"), Au-Ag-S phases, hessite, polybasite, and imiterite recognized at the prospect belong to the second mineral assemblage. The homogenization temperature of primary fluid inclusions in quartz ranges from 340 to 210 °C and decreased during the mineralizing process; fluid salinity varying from 0.8 to 5.2 wt% NaCl equiv is not evolved during the process. Cores of quartz crystals formed from a boiling fluid, whereas crystal rims appear to have formed from a lower temperature non-boiling liquid. LogfS_2 decreased from −8 at the formation of carbonate-base metal assemblage to −16 at the deposition of gold-silver-sulfosalt assemblage as temperature decreased from 340 to 200 °C. Bulk ICP-OES analysis of mineralized samples indicated up to: 38 ppm Au, 908 ppm Ag, 154 ppm Mo, 106 ppm Te, 53 ppm Se, 9246 ppm As, 1284 ppm Sb, and 23 ppm Bi. Cluster analysis of the data obtained identified three geochemical associations corresponding the carbonate-base metal the gold-silver-sulfosalt, and to the overlapped mineral assemblages. The whole-ore composition is controlled by mineralogy of these assemblages. Taking into account the geological setting, mineralogy, composition of minerals, and fluid inclusion data, the Tumanny Au-Ag-Te-Hg prospect is characterized as intermediate sulfidation epithermal style.

1. Introduction

The Tumanny epithermal prospect described here is 225 km south-southeast of Bilibino town, Chukotka Autonomus Okrug, Russia (Fig. 1, inset). The prospect is 40 km southeast of the Baimka Cu-Mo-Au porphyry trend, which includes the Peschanka porphyry copper deposit and Nakhodka district with several porphyry copper, and intermediate sulfidation (IS) epithermal gold deposits, as well as small low sulfidation (LS) epithermal gold occurrence (Nikolaev et al., 2016; Marushchenko et al., 2017). Both deposits as well as the Tumanny prospect are located within the Oloy tectonic zone of the Verkhoyansk-Chukotka folded area (Fig. 1). The deposits are spatially and genetically related to the plutons of the Early Cretaceous Egdykgich Complex, with U/Pb zircon age of 139–143 Ma (Moll-Stalcup et al., 1995; Kotova et al., 2012; Baksheev et al., 2014) and composed of monzonitic rocks. The Tumanny prospect is situated near the contact zone of the Vuknei pluton of the Egdykgych Complex and 30–40 km north of the boundary of the Okhotsk-Chukotka volcanic belt (Fig. 1). This volcanic belt (3200 km in length) is Albian to Campanian in age (Belyi, 1977; Filatova, 1988; Ispolatov et al., 2004; Hourigan and Akinin, 2004) and hosts many IS epithermal gold deposits, for example the Kupol and Dvoinoi mines now active, and the abandoned Karamken deposit.

This paper is an initial description of ore mineralogy and mineral chemistry (sulfides, tellurides, Au-Ag alloys), fluid inclusion

* Corresponding author.
E-mail address: baksheev@geol.msu.ru (I.A. Baksheev).

https://doi.org/10.1016/j.oregeorev.2018.06.021
Received 21 November 2017; Received in revised form 23 June 2018; Accepted 30 June 2018
Available online 02 July 2018
0169-1368/

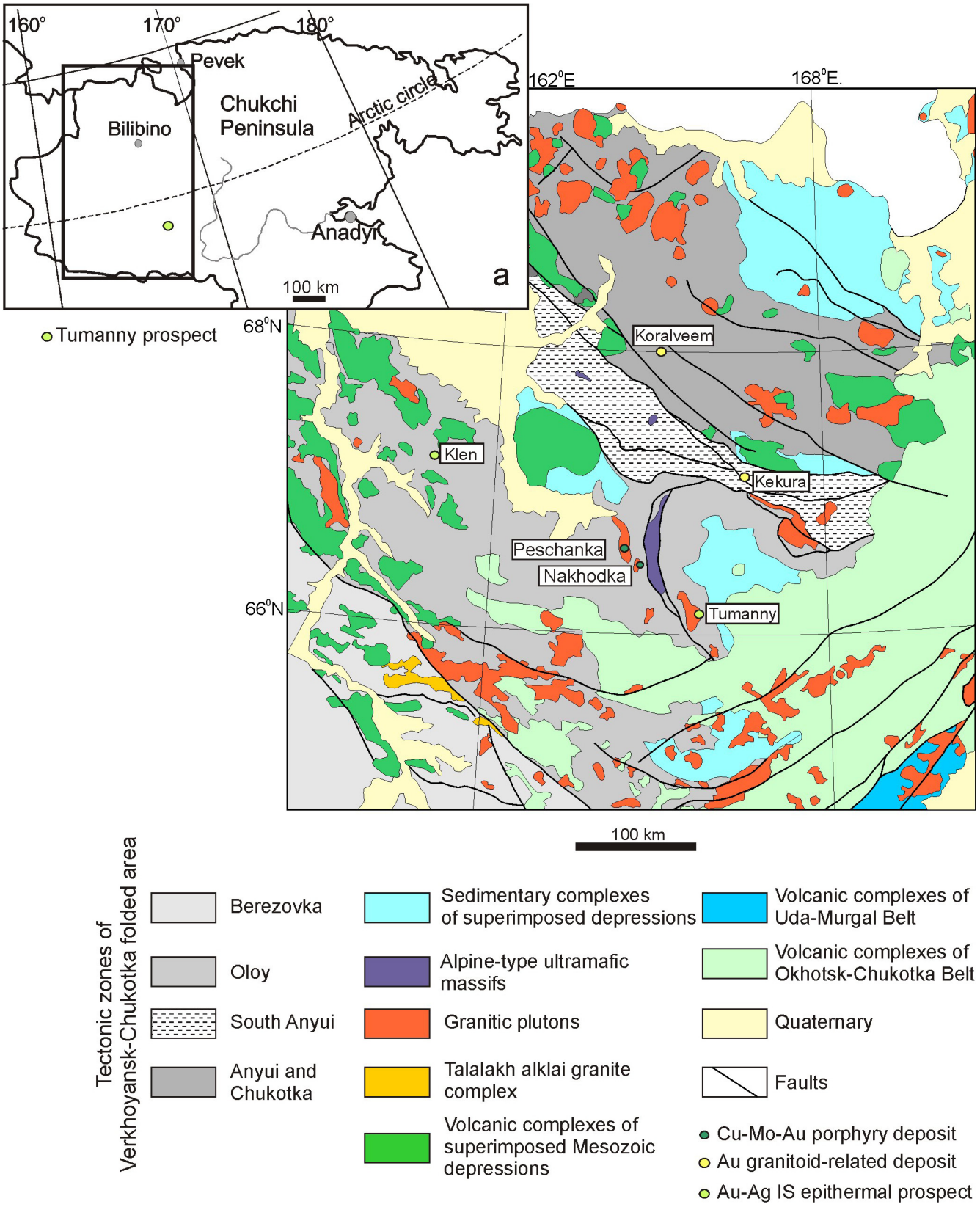

Fig. 1. Geological sketch map of western Chukotka, simplified after Tikhomirov et al. (2017). Geographical location of the Tumanny prospect is shown in the insertion.

characteristics in vein quartz, and bulk ore geochemistry of the Tumanny prospect. The epithermal mineralization is remote from the Baimka Cu-Mo-Au porphyry trend, but is spatially and possibly paragenetically related to the pluton of the Egdykgich Complex that is also associated with the Peschanka deposit and Nakhodka district (Nikolaev et al., 2016).

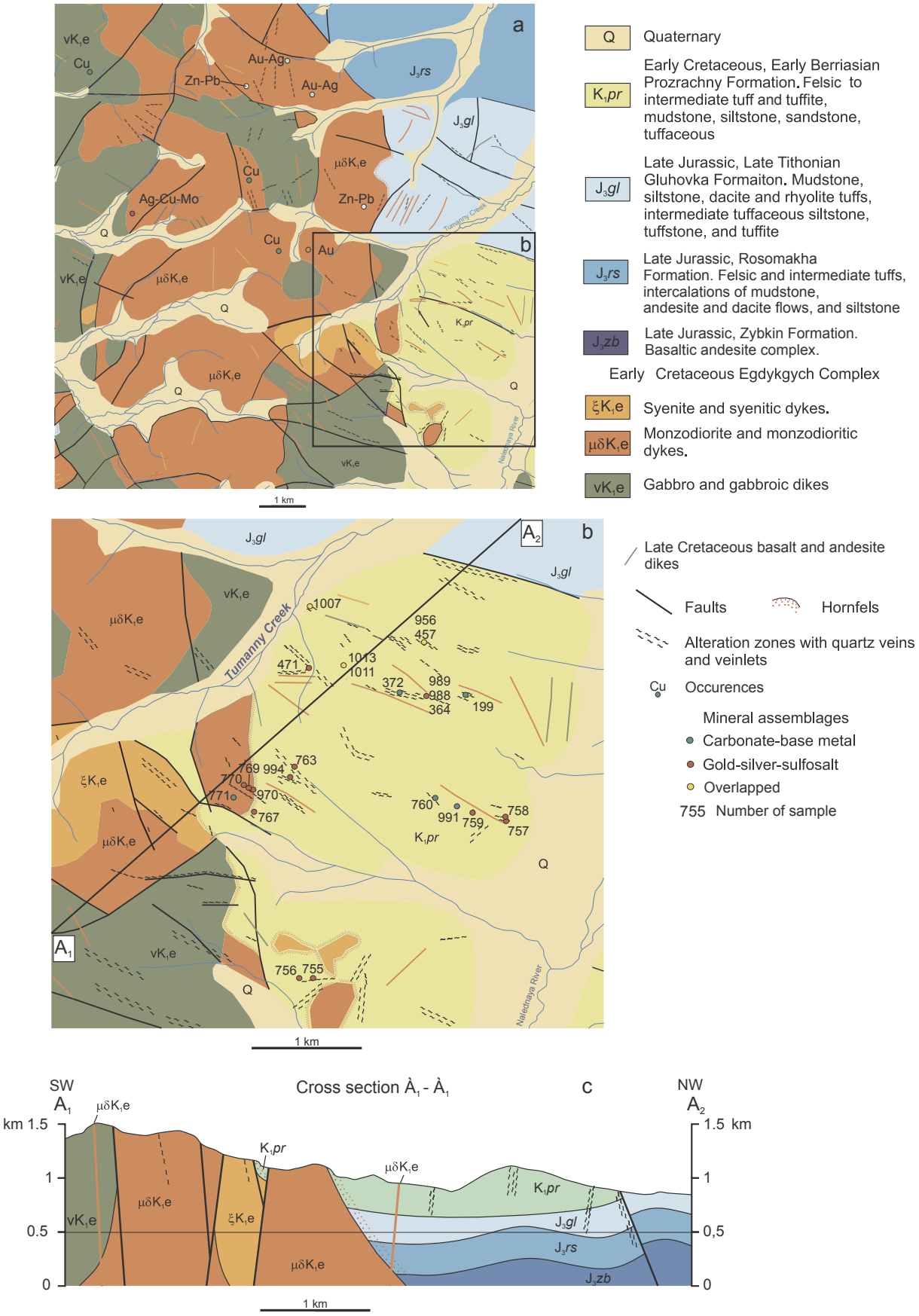

Fig. 2. Geological maps of (a) Vuknei ore district and (b) Tumanny prospect, and (c) geological cross section of the Tumanny prospect, modified after the data the Anyui Geological Exploration Expedition.

2. Brief geology

The Tumanny prospect is located within the Vuknei district 71 km^2 in area, which includes some copper, gold, and base-metal occurrences (Fig. 2a). The district is spatially related to the central and eastern contact of the Vuknei pluton that is a portion of the Early Cretaceous Egdykgych Complex. The Vuknei pluton intruded volcanic and terrigenous sequences of the Early Berriasian Prozrachny Formation, the Late Tithonian Glukhovka Formation and the Late Jurassic Rosomakha and Zybkin Formations (Fig. 2).

The Tumanny prospect is located near the eastern contact zone of the pluton (Fig. 2b, c). To date neither ore district nor prospect are explored and all samples studied have been collected from outcrops. The geology of the prospect comprises volcanic and terrigenous rocks of the Prozrachny Formation, which are intercalated felsic to intermediate tuff and tuffite, and mudstone, siltstone, and sandstone. Three intrusive phases of the pluton occur in the western part of the prospect: first-phase gabbroic rocks, second-phase porphyry monzodiorite and quartz monzodiorite, and third-phase syenite. In addition, numerous northwest trending gabbroic, monzonitic and syenite dikes up to a few hundred meters long and oriented northwest cut the Prozrachny sequence (Fig. 2b, c). Like Peschanka and Nakhodka district, the latest magmatic bodies at Tumanny are the north-trending Late Cretaceous fresh basalt and andesite dikes (Fig. 2b). Both Egdykgych and Prozrachny rocks are cut by faults parallel to the dikes. Propylitic alteration is the most abundant alteration style at the prospect and forms halos of a few ten meters thick around NW-, NE-, EW-, and NS-trending veins. Close to veins, the host rocks are sericitized to a thickness of a few meters, and silicification is developed adjacent to the veins. Sericite, quartz, and albite dominates the sericitic alteration. Quartz is predominant mineral in silicified rocks. There are no clay minerals in sericitic alteration and silicified rocks. The NW-trending veins predominate and are parallel to the dikes and faults. Steeply dipping mineralized and barren quartz veins are traced for up 800 m in the central and northern parts of the prospect. The similar quartz veins crosscut monzonitic rocks and gabbro of the Vuknei pluton and some samples were collected from them (Fig. 2b)

3. Analytical techniques

All samples for mineralogical, fluid inclusion, and geochemical studies were collected from natural outcrops at elevations of 720–1140 m above sea level.

3.1. Optical microscopy and electron microprobe

A microscopic study was performed on an Axioplan Zeiss microscope equipped with a digital photo camera and computer at the Division of Mineralogy, Moscow State University.

The chemical composition of minerals was measured with a Jeol JSM-6480LV SEM equipped with an INCA-Energy 350 EDS with an Si–Li solid-state detector at the Laboratory of High Spatial Resolution Analytical Techniques, Division of Petrology, Moscow State University, analysts N.N. Koshlyakova and V.O. Yapaskurt. The results were processed with the SEM Control User Interface v. 7.11 (Jeol Technics LTD) and INCA v. 17a (Oxford Instruments). The chemical composition was measured at an accelerating voltage of 20 kV, current intensity of 2nA, and beam diameter of 1–3 μm. The detection limit and relative uncertainty of a single measurement range from 0.05 to 0.5 wt% depending on the concentration and excitation energy of spectral lines used in measurements. The absolute uncertainty of a single measurement does not exceed 1.5% for the major constituents and up to 10% for admixtures. The following natural and synthetic sulfides and tellurides were used as reference materials: sphalerite (S, Zn), Mn metallic (Mn), chalcopyrite (Fe, Cu), arsenopyrite (As), alloy $Ag_{25}Au_{75}$ (Ag, Au), stibnite (Sb), PbTe (Te), PbSe (Se), and Bi_2S_3 (Bi).

3.2. Microthermometry

Fluid inclusions were studied in twice-polished plates of quartz about 0.3–0.5 mm in thickness, first optically at room temperature, then with a Linkam THMSG-600 freezing/heating stage equipped with an Olympus BX51 optical microscope, video camera, and computer at the Institute of Geology of Ore Deposits, Mineralogy, Geochemistry, and Petrography, Russian Academy of Sciences, Moscow, Russia. The chemical composition of fluid entrapped in inclusions was estimated from phase transitions and transformations during heating and freezing. The measurement uncertainty is 0.2 °C in the range of −20 to +20 °C and decreases beyond this range. The composition of salts predominant in fluid inclusion solutions was estimated from the eutectic temperature (Crawford, 1981). The salinity was estimated from final melting temperatures of ice according to experimental data on the NaCl–H_2O system (Bodnar and Vityk, 1994). Salinity and density of fluid were calculated with the FLINCOR program (Brown, 1989).

3.3. Cathodoluminescence

Cathodoluminescence (CL) study of quartz has been performed on a Cameca MS-46 electron microprobe optical system of which has been adapted and modernized to the high resolution CCD digital camera produced by Videoscan LLC, Russia at the Laboratory of Mineral Analysis, Institute of Geology of Ore Deposits, Petrography, Mineralogy, and Geochemistry, Russian Academy of Sciences, analyst O.M. Zhilicheva. CL was exited with electron beam in vacuum at room temperature and was registered as a bitmap image 300 × 300 μm in size at acceleration voltage 20 kV and current intensity 50 nA. The exposure time of one image was 240 s.

3.4. Whole-ore chemical analysis

Bulk chemical analysis of samples selected from quartz veins has been performed at the certified laboratory Stuart Geochemical and Assay, Moscow, Russia. The analysis included fire assay with atomic absorption finish (detection limit 10 ppb) for Au and ICP-OES spectrometry for 40 elements. The latter was performed after four acid (HCl-HNO_3-HF-$HClO_4$) digestion. Detection limits of the major ore and associated elements are (ppm): 0.5 Ag, 5 As, 5 Bi, 1 Cd, Cu, Mn, Mo, and Zn, 100 Fe, 2 Pb, 5 Sb, 10 Se and Te. Samples containing more than 1% Cu were repeatedly dissolved in HBr and analyzed with ICP-OES to improve determination of the Cu content. The accuracy of concentration measurements was 5%. Systematic and random uncertainties are over the range of $1.13 > \delta_{syst} > 0.84$ and $1.32 > \delta_{random} > 1.0$, respectively.

The data obtained were statistically processed with the Gold-Digger software package (Vorobiov, 2000) for clustering of the data set, separation of geochemical assemblages, and construction of correlation dendrograms.

4. Results

The mineralization at the Tumanny prospect occurs in the form of medium- to coarse-grained massive or cavernous quartz veins and veinlets with rare carbonate pockets and irregular disseminated sulfide minerals (Fig. 3). Hypogene sulfide minerals reach 1 cm in size and their content ranges from 1 to 20 vol%. Pyrite, chalcopyrite, galena, sphalerite, and tennantite-tetrahedrite solid solution series (Ttr_s) are the major constituents; arsenopyrite, bournonite, acanthite I, polybasite, imiterite, hessite, Au-Ag-Te phase probably petzite, cervelleite, and Au-Ag alloys ("küstelite" and electrum) occur in minor amounts. Electrum is the major Au carrier, and Ag is present in Au-Ag alloys and hessite, Ttr_s, acanthite, imiterite, and petzite. Supergene or extremely low-temperature hydrothermal constituents include rare high-fineness gold, acanthite II, Ag_3S and Au-Ag-S phases, and the chalcocite group

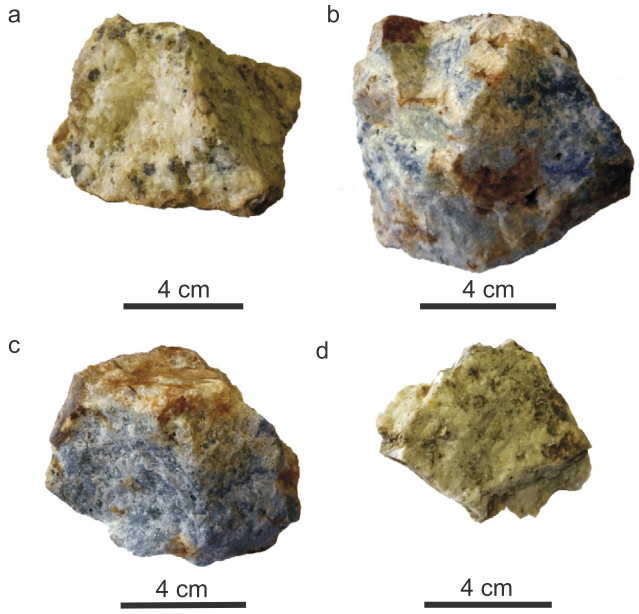

Fig. 3. Photographs of ore samples from the Tumanny prospect. (a) Carbonate-base metal ore, sample 372; (b, c) gold-silver-sulfosalt ore, samples 767 and 755; (d) overlapped carbonate-base metal and gold-silver-sulfosalt ore, sample 1007.

mineral.

Two mineral assemblages were identified in the ores: early carbonate-base metal and later gold-silver-sulfosalt. The two assemblages can be spatially separate, but in the most cases they are overlapped within the same zones and even within the same sample (Fig. 2b, 3d). Specific alteration related to the late assemblage was not observed; in both cases, veins are composed of massive to comb, milky to clear quartz (Fig. 3).

Paragenetic sequence of studied mineralization based on mineral assemblages, relationships between minerals, and chemical compositions of minerals indicates an early carbonate-base metal stage and later precious-metal epithermal stage, the latter consisting of two substages (Fig. 4).

4.1. Carbonate-base metal assemblage

Minerals of the carbonate-base metal assemblage are disseminated and occur as pockets in quartz veins (Fig. 3a). Pyrite, chalcopyrite, galena, and sphalerite are the major ore minerals; Ttr_s is minor. Gangue minerals are quartz, dolomite and calcite (Fig. 5a).

Pyrite is the most abundant mineral and is present in two generations. Pyrite I occurs as fine (10–150 μm) grains disseminated in quartz, strongly fractured elongated grains up to 1 mm in length, and isolated cubic crystals and aggregates of these crystals. Rims of large pyrite crystals contain local inclusions of later arsenopyrite. Electron microscopic study did not reveal compositional zoning in pyrite crystals. Contents of most trace elements in pyrite are below detection limits by electron microprobe (Table 1, anal. 1); only sporadic Cu contents (up to 0.4 wt%) are present. Pyrite II occurs as inclusions in Ttr_s of the carbonate-base metal stage (Fig. 5b). Similar pattern was previously described at the Darasun gold deposit in Transbaikal region and was considered as pyrite formation from chalcopyrite being replaced by Ttr_s according to reaction:

$10CuFeS_2 + 2As_2S_{3(fluid)} + 3S_{(fluid)} \rightarrow Cu_{10}Fe_2As_4S_{13} + 8FeS_2$ (Spiridonov et al., 2008).

Only Fe and S were detected in pyrite II using electron microprobe (Table 1, anal. 2).

Chalcopyrite is rarely disseminated in quartz as rare anhedral and rounded grains ranging from < 1 to 1.5 mm and from 50 to 100 μm in size, respectively. It overgrows early pyrite and is replaced by Ttr_s (Fig. 5b). In addition, chalcopyrite occurs as fine emulsion in sphalerite (Fig. 5d). The chemical composition of the mineral is, wt%: 34.23 Cu, 30.58 Fe, 35.10 S, total 99.91. Chalcocite group minerals replace chalcopyrite (Fig. 5c).

Sphalerite is intergrown with chalcopyrite (Fig. 5b) and is overprinted by galena (Fig. 5d). It occurs as grains up to a few mm in size with fine emulsion of chalcopyrite. The chemical composition of sphalerite is, wt%: 64.80–64.99 Zn, 0.64–0.94 Fe, 0.33–0.48 Cd, 0.17–0.18 Mn, bdl-0.80 Cu, total 98.97–99.44. The chemical formula calculated of the mineral on the basis of two atoms is $Zn_{0.918-0.926}Fe_{0.055-0.061}Cd_{0.003-0.004}Mn_{0.003}Cu_{0-0.012}S_{0.999-1.003}$.

Galena occurs as equant grains and clusters with pyrite, sphalerite, and Ttr_s of 0.1–1.0 and 3–4 mm in size, respectively, as well as, irregular-shaped pockets up to 1 cm across within quartz and fine inclusions in Ttr_s. Hessite and local Hg-bearing Au-Ag alloy and acanthite are enclosed in galena (Fig. 7a, c, f, 8d). Galena contains minor Se (0.3 wt %).

Tennantite-tetrahedrite solid solution overgrows and replaces chalcopyrite and pyrite (Fig. 5b, e). It includes rare bournonite and galena (Fig. 5f). Ttr_s grains reach 150 μm in size. The Sb/(Sb + As) (*sb*) versus Fe/(Fe + Zn) (*fe*) values range from 0.01 to 0.96 and from 0.03 to 0.20 respectively; the Cu_{excess} and Ag contents vary from 0 to 0.11 and from 0 to 0.20 apfu, respectively (Table 2, anal. 1–3; Fig. 6). A weak oscillatory zoning observed in some grains (Fig. 5g, h) is caused by variable contents of As and Sb.

Bournonite occurs as inclusions up to a few ten microns in Ttr_s (Fig. 5f). Its chemical composition is, wt%: 14.08 Cu, 40.49 Pb, 25.78 Sb, total is 99.98. The formula calculated based on 6 atoms is $Cu_{1.07}Pb_{0.94}Sb_{1.02}S_{2.96}$. We suggest that bournonite is resulted from the reaction between galena and Ttr_s, supported by the inclusions of galena in Ttr_s (Fig. 5f).

4.2. Gold-silver-sulfosalt assemblage

Minerals of the gold-silver-sulfosalt assemblage are disseminated in massive fine- to medium-grained quartz veins (Fig. 3b, c). This assemblage is composed of As-bearing pyrite III, arsenopyrite, galena, tennantite-tetrahedrite solid solution, native gold, Au-Ag alloys (electrum and “küstelite”), polybasite, acanthite, imiterite, and the Au-Ag-S phases.

As-bearing pyrite III, the major sulfide in the assemblage, is irregularly disseminated in vein quartz. It occurs as isolated crystals ranging from a few hundred μm to 1 mm and less frequent small pods up to 2 mm in diameter. Pyrite III also, forms acicular crystals up to 200 μm in length, (possible pseudomorphs after pyrrhotite or marcasite) overprinted by arsenopyrite (Fig. 7a). The oscillatory zoning caused by the variable As concentration is visible in a back-scattered electron (BSE) image (Fig. 7b). Zoned pyrite enriched in As overgrows early As-free pyrite I. The As content in pyrite III reaches 5.1 wt% (Table 1, anal. 4).

Arsenopyrite overgrows elongated crystals of pyrite III and quartz (Fig. 7a), occurs as isolated spotty-zoned crystals up to 100 μm in length and sheaf-like aggregates of these crystals. Twined acicular crystals have been identified. Frequently, elongated crystals of arsenopyrite are overprinted by short prismatic crystals of arsenopyrite, which can be considered as the second generation of the mineral. Arsenopyrite of the first generation is zoned with cores locally enriched in Co and Ni up to 2.0 and 1.1 wt%, respectively (Fig. 7c; Table 1, anal. 6), The Sb admixture reaches 1.2 wt% (Table 1, anal. 5–7) in the crystal cores, but the cores enriched in Ni and Co are depleted in Sb (up to 0.4 wt%) (Table. 1, anal. 6).

Sphalerite occurs as euhedral grains up to a few dozen μm in quartz (Fig. 7d). The mineral does not contain chalcopyrite emulsion. It is enriched in Fe (16 mol% FeS) and Cu (8.3 wt%).

Galena forms euhedral grains up to a few hundred in quartz and

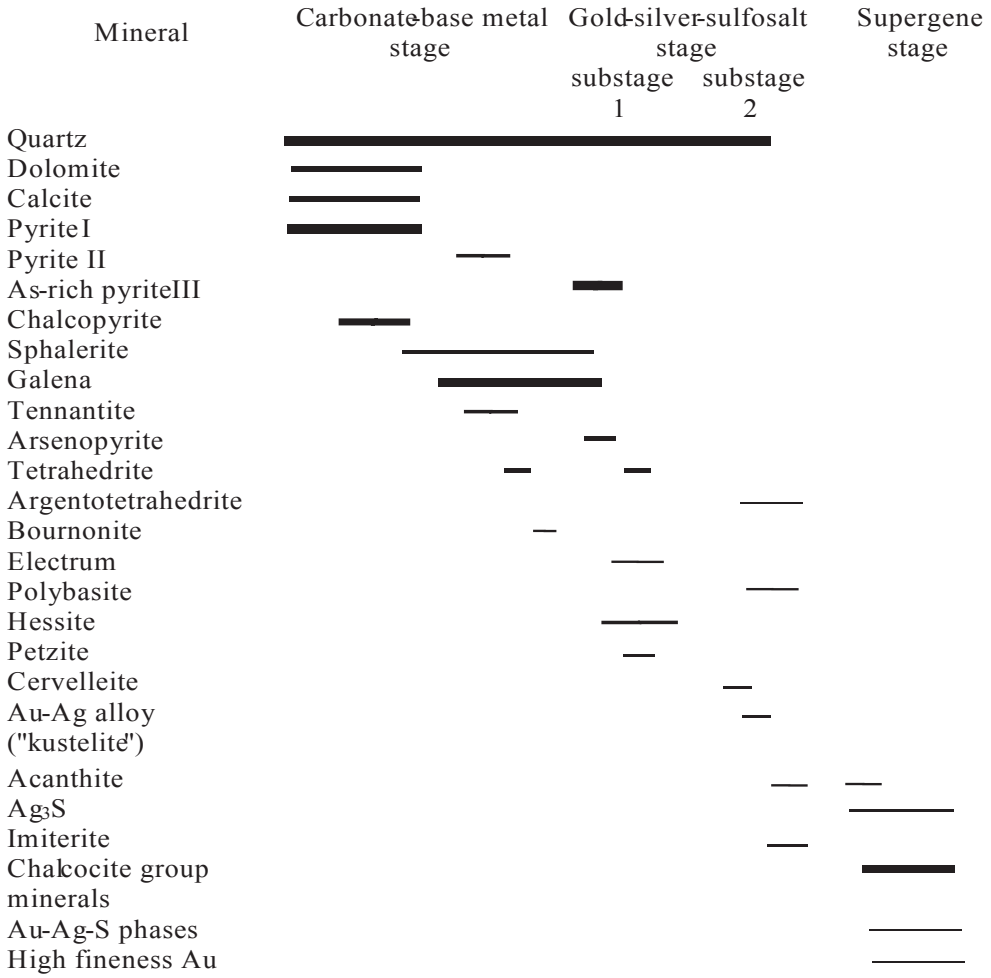

Fig. 4. Paragenetic sequence of ore minerals from the Tumanny prospect.

overgrows pyrite III (Fig. 8g); inclusions of galena were also identified in As-bearing pyrite.

Tennantite-tetrahedrite solid solution occurs as equant grains up to 300 μm in size in quartz; Ttr_s also replaces pyrite III. Compositionally, Ttr_s belongs to Zn-rich tetrahedrite and argentotetrahedrite (Table 2, anal. 4–7; Fig. 6). The *sb* and *fe* values range from 0.74 to 1.00 and from 0.03 to 0.22, respectively; the Ag content varies from 0.46 to 10.40 apfu (Fig. 6); there is no Cu_{excess}. A small excess of Ag is due to capture of acanthite, which fill fractures in argentotetrahedrite (Fig. 7e). Some grains display a weak mosaic zoning (Fig. 9) that is caused by isomorphic substitutions As ↔ Sb, Ag ↔ Cu, and Fe ↔ Zn. Ttr_s is replaced by acanthite (Fig. 7e).

Ag and Au-Ag tellurides. Hessite (Ag_2Te) is the major telluride mineral at the prospect. It replaces galena along fractures (Fig. 10a), occurs as inclusions (including those intergrown with electrum) varying from 5 to 20 μm in size (Fig. 10b) in pyrite III, and as isolated equant inclusions ranging from of 20 to 50 μm in size in galena (Fig. 10c). Also, this mineral forms aggregates 50–100 μm in size together with cervelleite and barite in quartz (Fig. 10d). *Cervelleite* (Ag_4TeS) replaces hessite (Fig. 10e). An Au-Ag-Te phase (probably *petzite* on the basis of qualitative data; Ag_3AuTe_2) is intergrown with hessite included in galena (Fig. 10f). The chemical composition of hessite is stoichiometric; cervelleite is characterized by an insignificant excess in Te and S deficiency (Table 3, anal. 5–9).

Au-Ag alloys occur as electrum and "küstelite". Electrum forms anhedral commonly elongated grains ranging from 5 to 70 μm in size embedded in As-bearing pyrite III (Fig. 8a), as well as, on the boundary between pyrite and quartz. It is intergrown with hessite (Fig. 10b); electrum forms the thinnest stringers and irregular-shaped segregations in the products of galena oxidation. The grains of electrum are unzoned; the fineness ranges from 598 to 675; the content of trace elements is below detection limit (Table 4). The largest grains of electrum are cut by very thin (< 1 μm thick) stringers of high-fineness native gold; the latter also rims electrum (Fig. 8b). Due to its finest size the chemical composition of this native gold could not be quantified. However, qualitative analysis showed a higher fineness as compared to the host electrum. Locally, electrum is rimmed by the phases in the Ag-Au-S system ranging from 1 to 15 μm (Fig. 8c) in width and zoned with decreasing Au content outward.

"*Küstelite*" (Ag-Au alloy) has been found as intergrowth with acanthite embedded in galena (Fig. 8d). The size of küstelite grains is about 10 μm and contains significant Hg, up to 9.25 wt% (Table 4, anal. 5).

Acanthite (Ag_2S) occurs as rare irregular-shaped grains in quartz up to 100 μm in size, replaces argentotetrahedrite along fractures, and is closely intergrown with "*küstelite*" (Fig. 8d). Two generations of acanthite occur with the first generation (acanthite I) intergrown with Ag-Au alloy (e.g. "küstelite") and containing oriented lamellae of the rare mineral imiterite (Ag_2HgS_2), up to 20 μm in length (Fig. 8e, Table 3, anal. 1) most likely resulting from exsolution. Acanthite I contains Hg, up to are 0.9 wt% (Table 3, anal. 2). The phase having a composition Ag_3S (Table 3, anal. 3, 4), overgrows acanthite-imiterite aggregates (Fig. 8h). It is characterized by up to 0.2 wt% Hg (Table 3, anal. 4). Acanthite II is disseminated in aggregates of supergene minerals.

Polybasite $(Ag,Au)_{16}Sb_2S_{11}$ is embedded together with galena and electrum in pyrite I, fills late fractures (Fig. 8f, h), and occurs as fine grains in quartz. The size of the mineral grains ranges from a few ten to

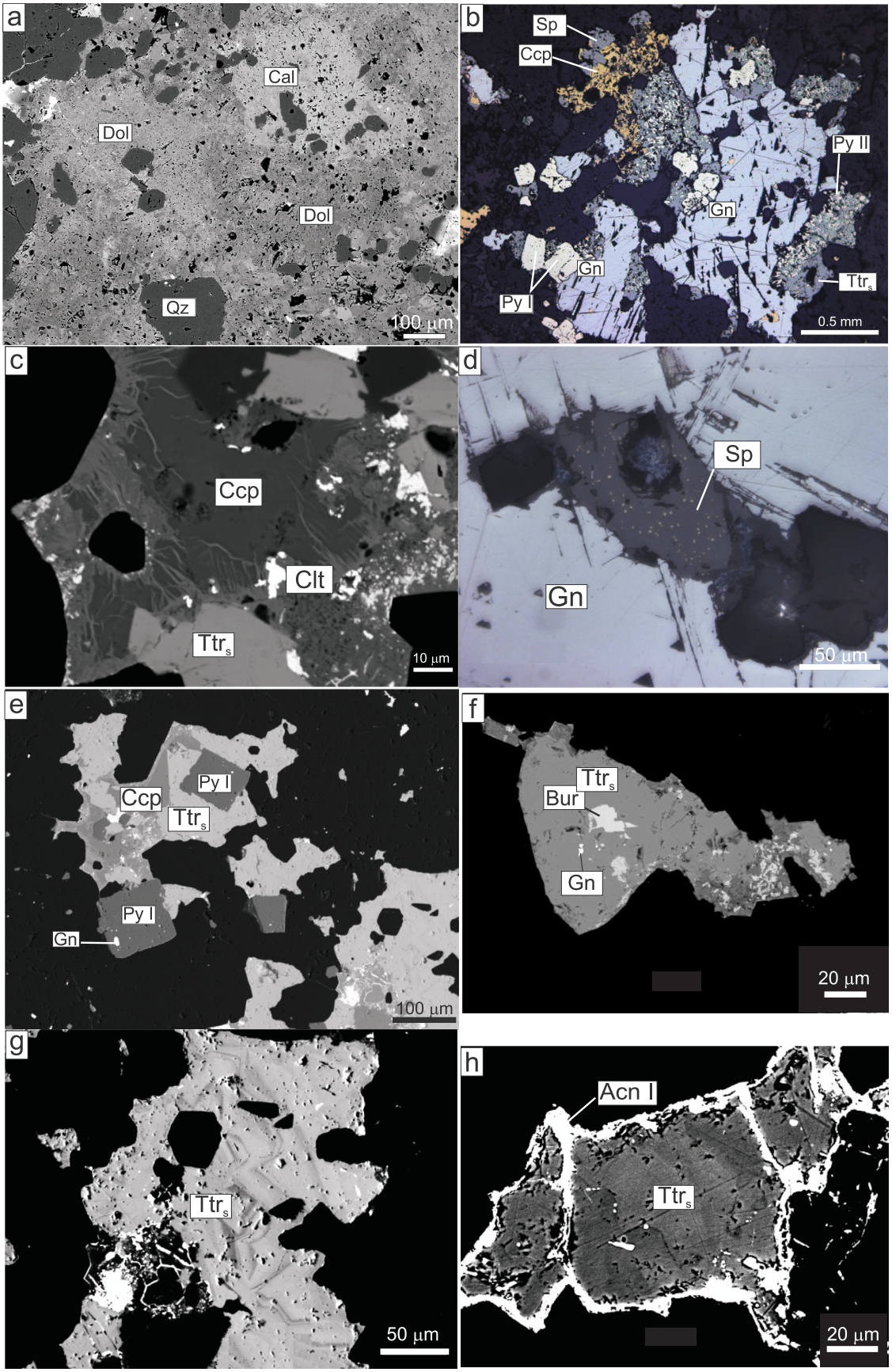

(caption on next page)

Fig. 5. Minerals of the carbonate-base metal assemblage. (a) Gangue constituents: quartz, calcite, and dolomite; (b) pyrite I, galena, and chalcopyrite, the last is replaced by tennantite-tetrahedrite solid solution (Ttr_s) to form pyrite II; (c) group chalcocite group mineral replaces chalcopyrite; (d) inclusion of sphalerite with disseminated chalcopyrite in galena; (e) Ttr_s replaces chalcopyrite and pyrite I; (f) inclusions of bournonite and galena in Ttr_s; (g, h) weakly oscillatory zoned Ttr_s grains. (a, c, e, f, g, h) Back-scattered electron images; (b, d) photomicrographs in reflected light. (Bur) Bournonite, (Ccp) chalcopyrite, (Gn) galena, (Py) pyrite, (Qz) quartz, (Sp) sphalerite, (Ttr_s) tennantite-tetrahedrite solid solution.

Table 1
Representative electron microprobe data for Tumanny pyrite and arsenopyrite.

Compon.	1 Py I	2 Py II	3 Py III	4 Py III	5 Apy	6 Apy	7 Apy
Fe, wt%	46.51	45.45	44.92	45.83	34.42	29.31	35.74
Co	bdl	bdl	bdl	bdl	bdl	1.99	bdl
Ni	bdl	bdl	bdl	bdl	bdl	1.09	bdl
S	52.76	52.09	48.62	51.91	20.07	17.20	24.78
As	bdl	bdl	5.15	1.62	45.51	51.25	40.21
Sb	bdl	bdl	bdl	bdl	1.15	0.37	0.16
Total	99.27	97.54	98.69	99.36	101.15	101.22	100.89
Formulae calculated on the basis of 3 atoms							
Fe	1.009	1.001	1.011	1.000	0.995	0.874	0.984
Co						0.056	
Ni						0.031	
S	1.991	1.999	1.903	1.974	1.010	0.894	1.189
As			0.086	0.026	0.980	1.140	0.825
Sb					0.015	0.005	0.002

Samples: 970 (1, 3, 5–7), 1013 (2), 755 (4). (Py) Pyrite, (Apy) arsenopyrite.

a few hundred μm. Polybasite contains Cu and Fe, 1.8 and 0.3 wt%, respectively (Table 2, anal. 8)

4.3. Fluid inclusions

Fluid inclusions (FI) were studied from 18 quartz samples, which include quartz containing carbonate-base assemblage, gold-silver-sulfosalt assemblage, and their overprint (overlapped assemblages). Petrographic study at room temperature revealed primary and secondary two-phase liquid-dominant aqueous inclusions (Fig. 11). In addition, in the crystal core vapor-phase inclusions (Fig. 11d) are present together with primary two-phase inclusions. The two-phase liquid-dominant and vapor-phase inclusions were possibly simultaneous trapped from boiling fluid. However, extremely low content of liquid in vapor inclusions prevents measurement of their homogenization temperature and simultaneous entrapment cannot be proved. Therefore below only two-phase liquid-dominant inclusions are described. Since quartz veins containing these assemblages are identical in its texture, we used cathodoluminescence (CL) to study one sample from each type (Fig. 12) to determine differences in vein quartz features.

Carbonate-base metal assemblage. The CL images of quartz from sample 760; 900 m above sea level (a.s.l.) containing only the carbonate-base metal assemblage show two quartz varieties. The first variety is zoned crystals with non-luminescent core and weakly luminescent thin zones close to the crystal margin (Fig. 12a). The second variety with stronger luminescence heals fractures in the first-variety quartz (Fig. 12b). We examined FI only from the first-variety quartz, because no inclusions suitable for microthermometry were present in the second variety. In the cores of the first-variety quartz crystals primary two-phase inclusions homogenized at 266–273 °C into liquid, respectively are present. In the crystal margin, primary two-phase inclusions homogenize into liquid at 263 °C. It should be noted that these temperatures are close to those measured in quartz from the later gold-silver-sulfosalt assemblage (Fig. 13a; Table 5). At the same time, homogenization temperature of primary two-phase liquid dominant inclusions in the cores of quartz crystals from samples 991, 956, and 771 collected at the elevation of 840, 1040, and 1080 m a.s.l., respectively containing only carbonate-base metal association is higher ranging from 307 to 342 and from 292 to 295 °C in the cores and rims, respectively (Fig. 13; Table 5). The substantial difference in homogenization temperature of fluid inclusions in quartz from sample 760; 900 m a.s.l. and other samples can be caused by that the crystals studied are later and have been precipitated during gold-silver-sulfosalt stage. This suggestion is supported by the fluid inclusion data from quartz of the gold-silver-sulfosalt stage (see below).

Fluid salinity in primary inclusions from all samples ranges from 1.2 to 2.5 wt% NaCl equiv (Fig. 13a, Table 5). Eutectic temperature ranging from −30 to −25 °C indicates that quartz crystallized from NaCl dominant fluid with possible admixture of divalent cations (Mg^{2+} or Fe^{2+}) (Crawford, 1981).

Secondary two-phase inclusions homogenized to the liquid phase at 200–230 °C. Fluid salinity and eutectic temperature ranged from 1.5 to 2.5 wt% NaCl equiv and from −30 to −27 °C, close to those measured in primary inclusions.

Gold-silver-sulfosalt assemblage. The CL images of quartz from sample

Table 2
Representative electron microprobe data for Tumanny tennantite-tetrahedrite solid solution and polybasite.

Compon.	1 Ttn	2 Ttn	3 Ttr	4 Ttr	5 Ttr	6 Ttrd	7 AgTtr	8 Plb
Cu, wt%	43.13	41.43	37.72	33.62	32.94	27.26	0.42	1.81
Ag	bdl	0.43	0.75	7.48	7.33	13.73	52.41	72.72
Fe	0.41	0.59	0.47	0.54	1.40	3.30	0.69	0.30
Zn	8.66	7.36	7.25	7.07	5.95	5.82	5.16	bdl
As	19.65	15.39	0.70	4.38	3.86	2.52	3.70	bdl
Sb	bdl	7.23	29.08	23.00	23.88	23.06	17.08	10.16
S	27.92	27.31	24.71	24.83	24.61	22.91	19.44	15.32
Total	99.77	99.74	100.68	100.92	99.97	98.60	98.90	100.31
Formulae calculated on the basis of 29 atoms								
Cu	10.085	9.973	9.900	8.827	8.751	7.576	0.139	0.650
Ag		0.061	0.116	1.157	1.147	2.248	10.212	15.403
Fe	0.109	0.162	0.140	0.161	0.423	1.044	0.260	0.123
Zn	1.968	1.722	1.849	1.804	1.537	1.572	1.659	
As	3.897	3.143	0.156	0.976	0.870	0.594	1.038	
Sb		0.908	3.984	3.152	3.312	3.345	2.948	1.907
S	12.941	13.031	12.855	12.923	12.960	12.621	12.744	10.917

(1–2) Carbonate-base metal assemblage, (3) combined carbonate-base metal and silver-sulfosalt assemblages, (4–8) gold-silver-sulfosalt assemblage. Samples: 1011 (1), 199 (2), 457 (3), 755 (4), 989 (5), 364 (6), 994 (7). (AgTtr) Argentotetrahedrite, (Ttn) tennantite, (Ttr) tetrahedrite, (Plb) polybasite.

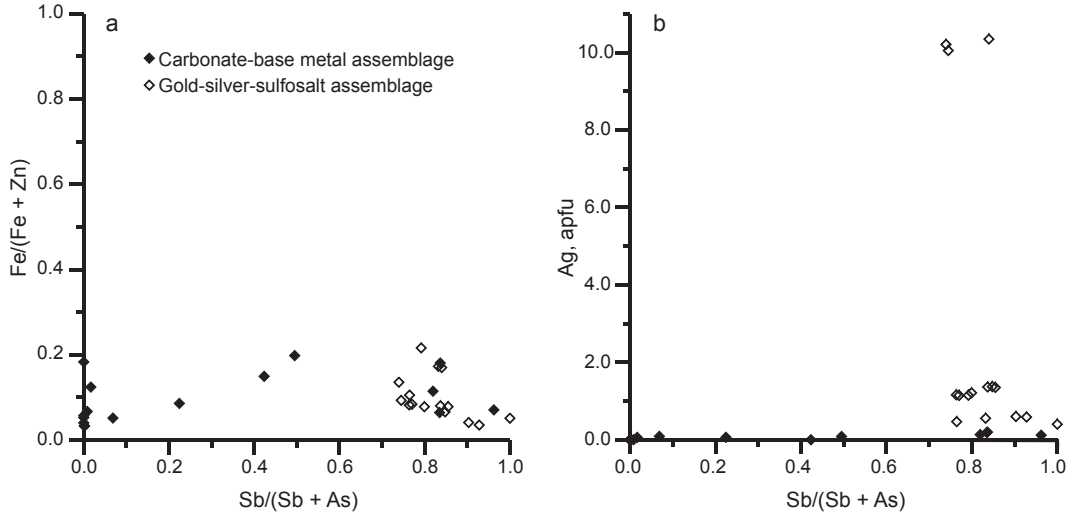

Fig. 6. Binary plots illustrating the chemical variations in the tennantite-tetrahedrite solid solution from the Tumanny prospect.

759; 800 m a.s.l. (with the gold-silver-sulfosalt association) also show two varieties. The first variety occurs as zoned crystals with non-luminescent core and weakly luminescent zones close to grain margins (Fig. 12c). Stronger luminescent second-variety quartz fills thin fractures in earlier quartz (Fig. 12d); therefore, no inclusions suitable for microthermometric study were found in this quartz. In sample 759, primary two-phase liquid-dominant inclusions from the first-variety quartz homogenized at 277 °C into liquid (Table 5). In quartz from another sample 758; 740 m a.s.l. containing gold-silver-sulfosalt assemblage, primary liquid-dominant inclusions homogenized at 265–278 and 210–214 °C were observed (Table 5). Temperatures of the first and second ranges were measured in the crystal cores and rims, respectively (Fig. 13a).

Fluid salinity in primary inclusions from all samples of this association ranges from 1.0 to 2.3 wt% NaCl equiv (Fig. 13a; Table 5). Eutectic temperature ranging from −32 to −30 °C is slightly higher than that of primary inclusions in quartz containing carbonate-base metal assemblage. Nevertheless, it indicates crystallization of the first-variety quartz from NaCl dominated fluid with possible admixture of divalent cations (Mg^{2+} or Fe^{2+}) fluid (Crawford, 1981). Secondary two-phase liquid-dominant inclusions homogenized into the liquid phase at 176 °C. Fluid salinity and eutectic temperature 2.8 wt% NaCl equiv and −30 °C (Table 5) are close to those measured in primary inclusions.

Overlapped assemblages. Quartz from sample 1011; 900 m a.s.l. containing both assemblages clearly shows two varieties in the CL images. The first variety occurs as zoned crystals with non-luminescent core and weakly luminescent thin zones close to the crystal margin (Fig. 12e). The second variety that healed fractures in quartz of the first variety and filled interstices between its crystals has stronger luminescence (Fig. 12f). We did not find fluid inclusions in the second variety in this sample so that only inclusions in variety 1 crystals were examined. In the crystal core two-phase liquid-dominated primary FI homogenized into liquid at 301 °C. In the crystal margins, primary FI homogenized at 283 °C.

Homogenization temperature of primary two-phase liquid dominant inclusions of quartz crystals from other samples 1013, 988, 767, 994, 755. 756, 763, 970, 769, and 770, collected at the elevation of 900, 920, 1000, 1020, 1080, 1100, and 1120 m a.s.l., respectively containing both assemblages ranges from 260 to 320 and from 230 to 290 °C in the crystal cores and rims respectively (Fig. 13). As is seen on the T_h versus salinity plot, one part of homogenization temperatures is close to range of temperature characteristic of quartz from veins containing carbonate-base metal assemblage and another part, to the range typical of quartz from vains containing later gold-silver-sulfosalt assemblage.

Fluid salinity in primary inclusions from the first-variety quartz in the other samples located at the elevation of 900 to 1120 m a.s.l. is low and similar to that in carbonate-base metal and gold-silver-sulfosalt assemblages (Fig. 13a, Table 5) ranging from 1.2 to 3.0 wt% NaCl equiv with the exception of sample 988; 920 m a.s.l. in which fluid salinity in inclusions from crystal rim is 5.2 wt% NaCl equiv. Eutectic temperature ranging from −24 to −31 °C indicates that quartz I crystallized from NaCl dominated fluid with possible admixture of divalent cations (Mg^{2+} or Fe^{2+}) fluid (Crawford, 1981). Secondary inclusions in the studied samples homogenized into liquid at 103–213 °C. Fluid salinity and eutectic temperature ranging from 2.6 to 3.4 wt% NaCl equiv and from −29 to −28 °C are close to those measured in primary inclusions.

Summarizing temperature and CL data for quartz from all vein types, we may conclude that there are at least three generations of quartz. The earliest quartz I with FI in the crystal cores homogenized at 310–340 °C corresponds to the carbonate-base metal stage. Later quartz II with FI in the crystal cores homogenized at 260–280 °C corresponds to the gold-silver-sulfosalt stage. According to the CL data, fractures in quartz I and quartz II are healed by quartz with stronger CL. This quartz may be considered as quartz III. It cannot be ruled out that homogenization temperatures of secondary FI (170–210 °C) measured in quartz I and II correspond to the formation temperature of quartz III. Salinities of fluids in primary inclusions from quartz I and II predominantly range from 0.8 to 3.3 wt% NaCl equiv; salinities of fluids in secondary inclusions range from 1.5 to 3.4 wt% NaCl equiv.

4.4. Whole-ore geochemistry

The results of ICP-OES and assay analyses of 111 samples from quartz veins of the Tumanny prospect show anomalous contents (g/t) of Au (37.6), Ag (908), Zn (9322), Pb (198000), Cu (18500), Mo (154), As (9246), Sb (1284), Se (53), Te (106), Cd (49.4), Bi (23) (Table 6). Cluster analysis showed that the data set is divided into four groups. Three groups consisting of 53 samples (47.7%) have an anomalous content of metals (Table 6). The fourth group consisting of 58 samples (52.3%) is characterized by low content of metals and is not discussed below. Each of the three groups consists of samples similar in composition and relationships of ore elements. Average contents (Table 6) and correlation dendrograms for each group (Fig. 14) allow identification of geochemical anomalies corresponding to the mineral assemblages.

The first group (18 samples) is characterized by high contents of Pb, Cu, Zn, Cd, and Ag vs. low contents of Au, As, Sb, and Mo (Table 6). Pb is the major element in this group; its average concentration is higher

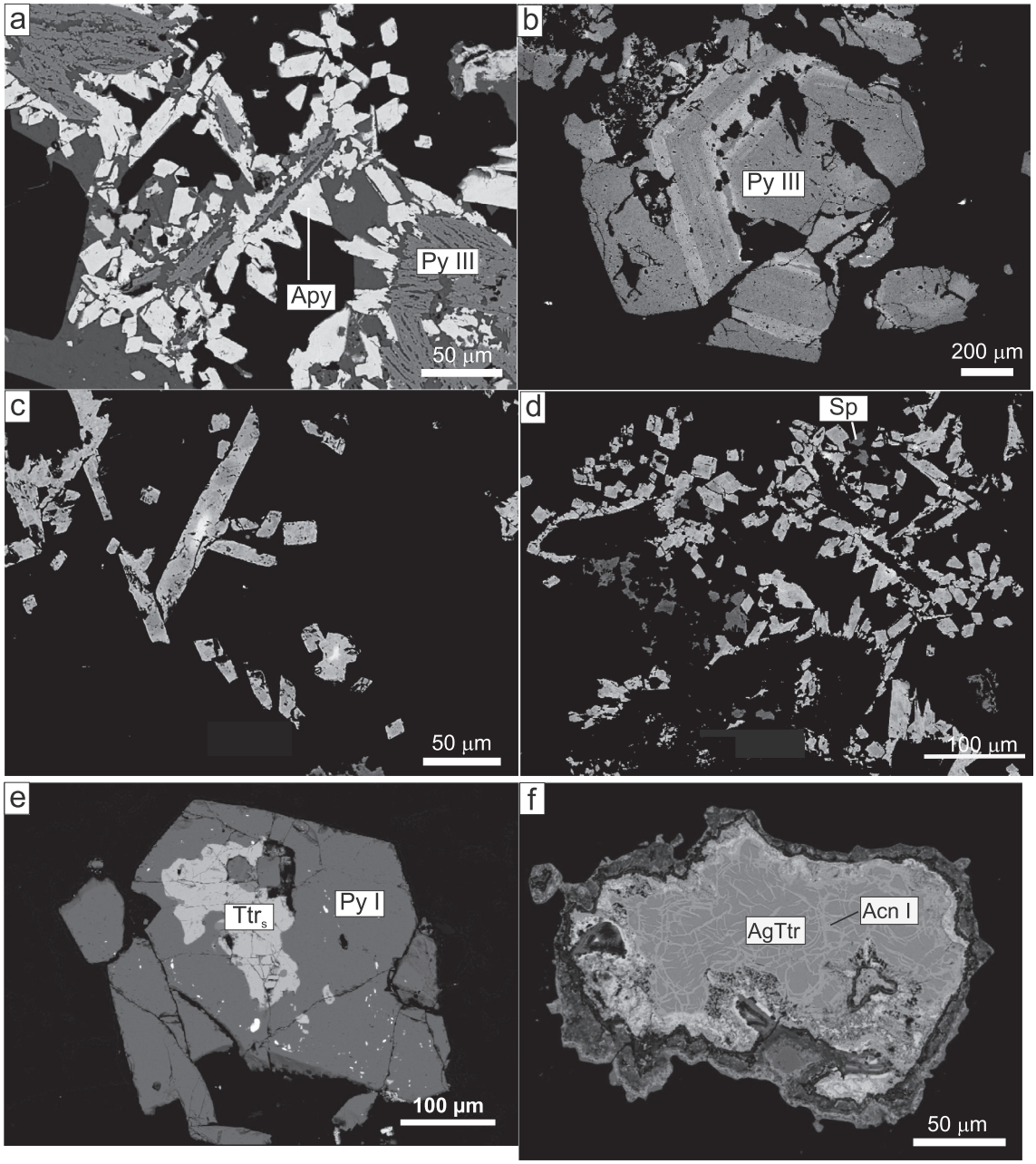

Fig. 7. Back-scattered electron images of minerals from gold-silver-sulfosalt and overlapped assemblages. (a) Elongated crystals of pyrite III overprinted by arsenopyrite, (b) oscillatory zoned As-bearing pyrite III, (c) isolated acicular spotty-zoned crystals of arsenopyrite, cores of some crystal are enriched in Ni and Co, (d) grains of sphalerite and arsenopyrite, (e) pyrite I replaced by Ag-bearing tetrahedrite, (f) grain of argentotetrahedrite replaced by acanthite. (Acn) Acanthite, (Apy) arsenopyrite, (AgTtr) argentotetrahedrite. See Fig. 5 for other abbreviations.

than 2000 ppm. Significant positive correlation ($r > 0.5$ at $r_{5\%} = 0.47$) and elevated contents (Fig. 14a, Table 6) indicate Ag, Cu, Zn, and Cd are associated with Pb. Au, As, Sb, and Mo have insignificant correlation between each other and are not related to base metals. These latter elements are likely impurities due to to the later stage.

The second group (15 samples) has elevated contents of Au, As, Sb, Mo, Pb, Cu, Zn, and Ag (Table 6). Gold is the major anomalous element in this group with average > 3 ppm associated with Fe, As, Sb, and Mo. Only Fe has a significant positive correlation with Au ($r > 0.6$ at $r_{5\%} = 0.5$) (Fig. 14b), whereas relationship of other associated elements and Au is below 5% confidence level. Nevertheless, they have constant elevated contents with Au The average and maximum contents of Pb, Cu, Pb, Zn, and Cd are lower than those in the first group.

The third group (20 samples) is characterized by high contents of Pb, Cu, Zn, and Cd, elements referred to the first geochemical assemblage, high concentration of As is referred to the second group, (Table 6). Ag, Au, and Pb are the major (in concentration level) elements. Cu, Zn, Cd, As, Cd, Sb, Te, and Se have strong positive correlations with them ($r > 0.7$ at $r_{5\%} = 0.44$) (Fig. 14c) and are considered as associated elements. Only Bi does not correlate with other ore elements and is considered as independent impurity.

5. Discussion

5.1. Mineralogical constraints

Tennantite-tetrahedrite group minerals and minor constituents in the mineralization, cervelleite, imiterite, Co-Ni bearing arsenopyrite

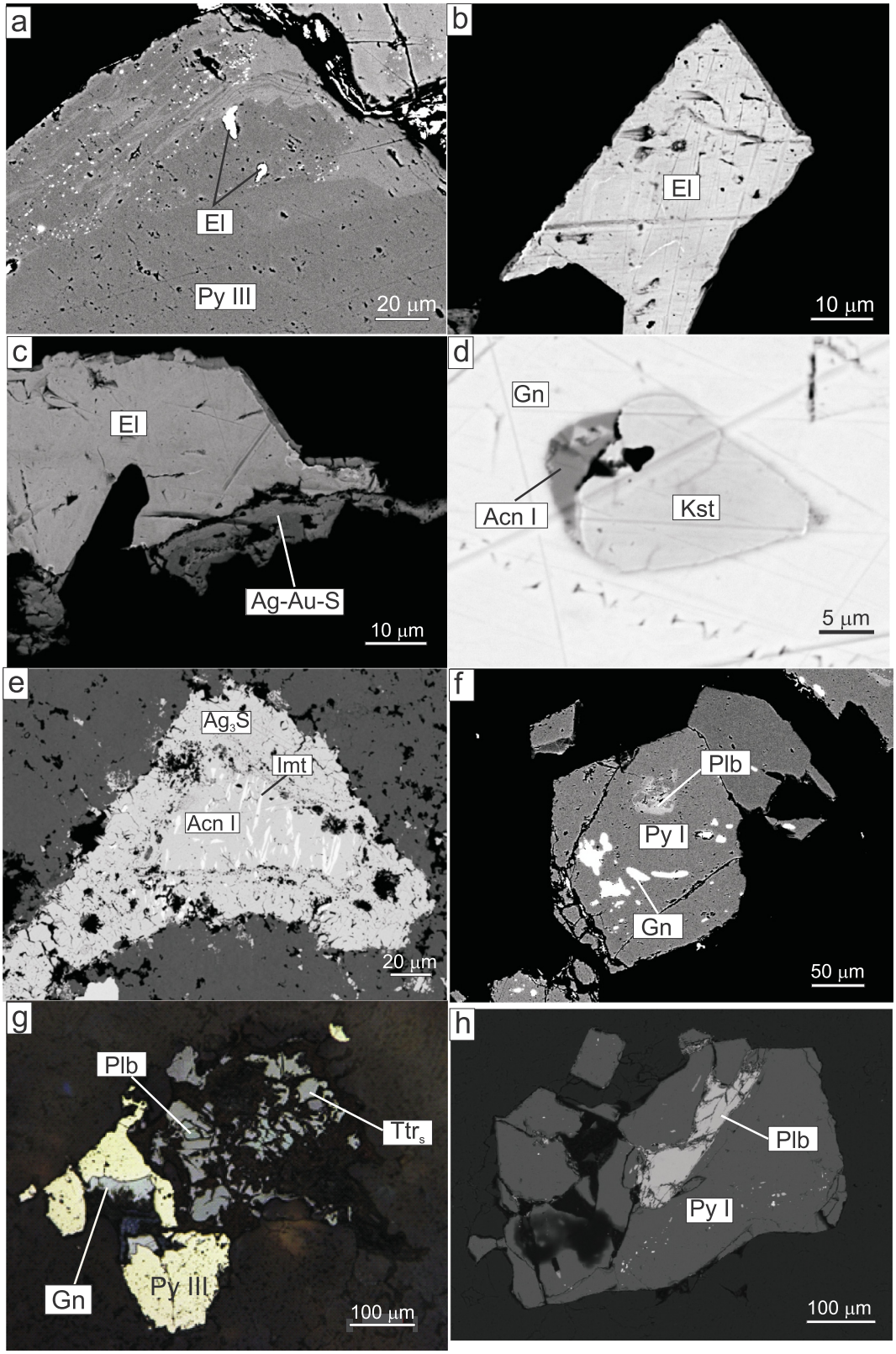

Fig. 8. Back-scattered electron images of precious metals-bearing minerals from the gold-silver-sulfosalts assemblage. (a) Inclusions of electrum in pyrite III; (b) inclusion of electrum in quartz, stringers of the higher fineness gold are visible (bright white), the grain of electrum is rimmed by the Au-Ag-S phase (gray phase, see also Fig. 8c for magnification); (c) electrum rimmed and replaced by a zoned Ag-Au-S aggregate, (d) intergrowth of Hg-bearing Au-Ag alloy ("küstelite") and acanthite in galena; (e) polybasite fills fracture in pyrite I, (f) inclusions of polybasite and galena in pyrite I; (g) polybasite cementing brecciated Ttr_s and galena overgrowing pyrite III, photomicrograph in reflected light; (h) acanthite grain with oriented exsolution lamellae of imiterite is rimmed by the Ag_3S phase. (Imt) Imiterite, (Plb) polybasite. See Figs. 5 and 7 for other abbreviations.

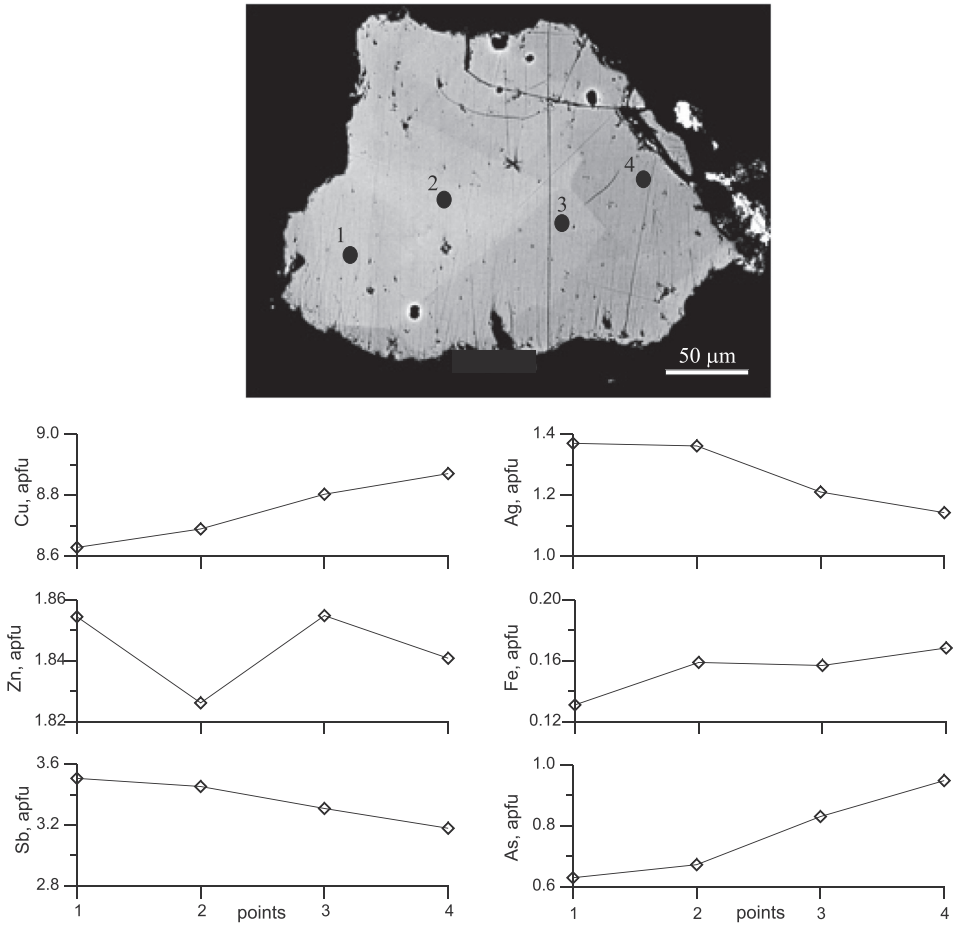

Fig. 9. Zoned grain of Ag-bearing tetrahedrite.

and Hg-rich phases may inform us on the physicochemical conditions of ore formation at the Tumanny prospect.

The chemical composition and zoning of the Ttr_s from the carbonate-base metal stage are identical to those found at the Peschanka and Nakhodka porphyry deposits (Marushchenko et al., 2017). According to these authors, Ttr_s from the carbonate-base metal veins at Peschanka, Nakhodka and from most porphyry deposits worldwide is characterized by oscillatory zoning caused by variable contents of Sb and As, a low Ag content and Fe/(Fe + Zn) value, and widely variable Sb/(Sb + As) values similarly to the Tumanny Ttr_s. However, it is noteworthy that Voudouris et al. (2006) reported Ag-rich tetrahedrite (1.526 apfu Ag) from carbonate-base metal veins at the Koryfes Hill porphyry type prospect.

Tetrahedrite from the gold-silver-sulfosalt stage at Tumanny has a similar chemical composition to tetrahedrite in epithermal IS (intermediate sulfidation) and differs from those at HS (high sulfidation) deposits (Carrillo-Rosúa et al., 2008; Fadda et al., 2005; Kovalenker et al., 1986; Marushchenko et al., 2017; Plotinskaya et al., 2014; Voudouris et al., 2013). In most cases, Ttr_s of HS mineralization is characterized by widely variable Sb/(Sb + As) and Zn/(Zn + Fe) values with a trend from Fe-rich tennantite to Zn-rich tetrahedrite and is Ag-poor. Nevertheless, Voudouris (2011) described Ag-rich tetrahedrite from the silver-bearing HS mineral assemblage at the Mavrokoryfi prospect in Greece. The IS tennantite-tetrahedrite in the Nakhodka district is Zn-rich and contains up to 4.1 wt% Ag (Marushchenko et al. 2017). The composition of the tetrahedrite group minerals from the gold-silver-sulfosalt stage at Tumanny resembles that from the IS epithermal Pb-Zn-Ag mineralization at the Kastimoutis prospect in Milos Island, Greece, where Ag-bearing tetrahedrite contains 7.6–29.4 wt% Ag (Alfieris and Voudouris 2005; Alfieris et al. 2013). Tetrahedrite-tennantite solid solution series are commonly absent from typical low sulfidation epithermal mineralization, where silver is mostly associated with Se-bearing phases, as for example at LS assemblages in the Baimka Cu-Mo-Au porphyry trend composed of chalcopyrite, low-fineness native gold, acanthite, naumannite, Se-bearing pearceite and arsenopolybasite (Nikolaev et al., 2016).

Cervelleite at Tumanny is closely associated with other Ag-bearing phases such as acanthite, küstelite, and imiterite and was formed during substage II mineralization, following crystallization of Au-Ag-Te phases (e.g. electrum, hessite, and petzite). Cervelleite was reported for the first time from the Bambolla Au-Te deposit in Mexico (Criddle et al., 1989). Later it was described from various ore types (Bindi et al., 2015; Voudouris et al., 2011 and references therein). The formation of cervelleite is considered to be resulted from reaction between acanthite and hessite (Criddle et al., 1989). At the Tumanny prospect, cervelleite replaces hessite and no acanthite was found in contact to to hessite. Its formation indicates decreasing tellurium and increasing sulfur fugacity of the late-stage hydrothermal fluids. According to information taken from Voudouris et al. (2011 and references therein), cervelleite-like sulfotellurides can be formed from hydrothemal fluids over a wide range of temperatures (< 100–420 °C) and $\log fTe_2$ values (−23 to −13.4). However, at the Kallianou Pb-Cu-Au-Ag vein deposit in Greece, cervelleite-like phases crystallized at $\log fTe_2$ from −19.5 to −15 and temperature around 200 °C. We assume that these conditions might be applied to the formation of cervelleite from Tumanny, since cervelleite overgrows and replaces hessite, and was formed very late in the paragenetic sequence from hydrothermal fluids probably at temperature in the range of 160 to 185 °C (e.g. homogenization temperature of secondary inclusions in quartz from the gold-silver-sulfosalt assemblage).

These temperature conditions are in accordance with the presence

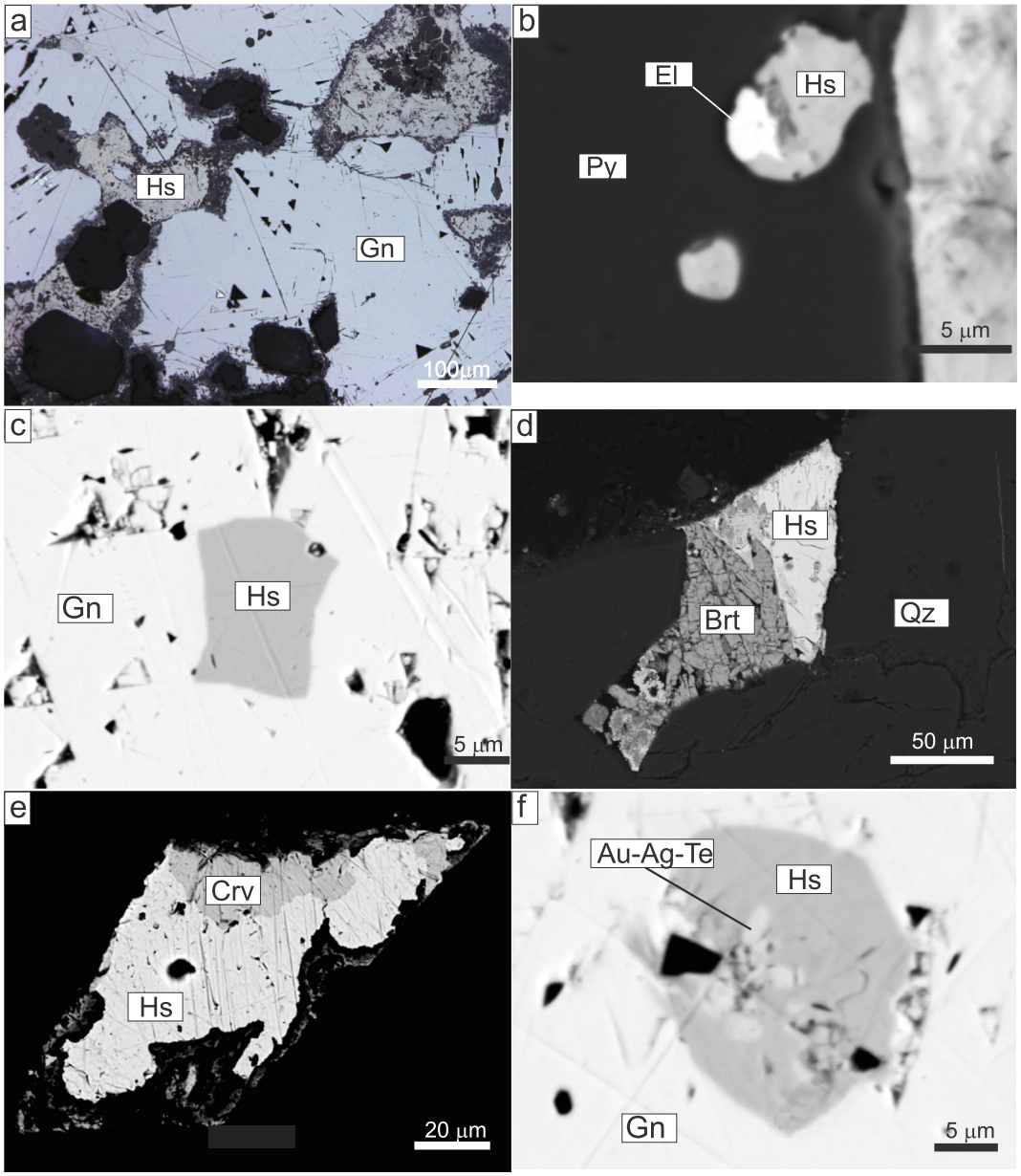

Fig. 10. Photomicrograph and back-scattered electron images of hessite from the gold-silver-sulfosalt assemblage. (a) Hessite replaces galena along fractures, (b) hessite-electrum intergrowth in pyrite, (c) inclusion of hessite in galena, (d) intergrowth of barite and hessite in quartz, (e) cervelleite replaces hessite, (f) inclusion composed of hessite and petzite (?) in galena. (a) Photomicrograph in reflected light, (b-f) back-scattered electron images. (Brt) Barite, (Crv) cervelleite, (El) electrum, (Hs) hessite, (Au-Ag-Te) Au-Ag-te phase. See Figs. 5 and 10 for other abbreviations.

of imitetrite in the latest-stage ore paragenesis at Tumanny, and are consistent with imiterite formation from other known occurrences elsewhere. At the giant epithermal Ag-Hg ore deposit at Imiter in Morocco (Guillou et al., 1985), imiterite was precipitated at the late stage in association with Ag–Hg amalgam, argentite, polybasite, pearceite, tetrahedrite-tennantite, proustite-pyrargyrite, acanthite, arsenopyrite, pyrite, and galena (Levresse et al., 2016). This assemblage is similar to that where imiterite was found at the Tumanny prospect. According to Levresse et al. (2016), the imiterite-bearing assemblage has been formed at ~180 °C and 1.9–0.9 kbar from a fluid with salinity ~10 wt% NaCl equiv. This temperature is close to the homogenization temperature of secondary inclusions in quartz from the Tumanny prospect. However, fluid salinity and pressure are much higher at Imiter. The Khaak-Sair gold prospect, Western Tuva, Russia is another example of the deposits, where imiterite has been found. At Khaak-Sair, imiterite enriched in Se is associated with gersdorffite, naumannite enriched in Hg, bornite, Hg-bearing native gold, and galena-clausthalite solid solution. According to Kuzhuget et al. (2015), this assemblage have been formed at 130–230 °C, which is similar to that at the Imiter deposit and is consistent with the range of homogenization temperature of secondary inclusions at Tumanny.

The Tumanny prospect is characterized by Hg enrichment, in common to other prospects spatially related to the Egdykgych rocks. Cinnabar associated with marcasite is present at the Pryamoi prospect located within the Nakhodka porphyry copper deposit. In addition, cinnabar was found from the gold placer in the Pravy Svetly Creek that erodes a porphyry copper prospect situated about 55 km north of Tumanny and related to the Egdykgych Complex (A.F. Chitalin, pers. communication). Mercury was partitioned into a rising vapor phase during probable boiling (taking into account vapor-phase inclusions in quartz) of the epithermal fluids at Tumanny, similarly to that suggested for the Pueblo Viejho precious metal deposits, Dominican Republic

Table 3
Representative electron microprobe data for Tumanny Ag minerals.

	1 Imt	2 Acn	3 Ag_3S	4 Ag_3S	5 Hs	6 Hs	7 Hs	8 Crv	9 Crv
Ag	47.13	85.53	89.31	88.87	61.68	63.90	63.08	71.99	71.48
Hg	40.18	0.89	bdl	0.19	bdl	bdl	bdl	bdl	bdl
S	14.26	12.76	9.74	9.82	bdl	bdl	bdl	5.11	4.78
Te	bdl	bdl	bdl	bdl	36.56	37.08	37.16	22.29	23.35
Total	101.57	99.17	99.04	98.88	98.24	100.98	100.24	99.39	99.61
Formulae									
Ag	2.019	1.990	2.927	2.914	1.998	2.012	2.003	3.999	3.997
Hg	0.926	0.011		0.003					
S	2.055	0.999	1.073	1.083				0.955	0.899
Te					1.002	0.988	0.997	1.047	1.104

Calculation of apfu values normalized on, atoms: 5 imiterite, 3 acanthite and hessite, 4 Ag_3S, and 6 cervelleite. Samples: 364 (1–4), 769 (5), 783 (6), 1013 (7–9). (Acn) Acanthite, (Crv) cervelleite, (Hs) hessite, (Imt) imiterite.

Table 4
Representative electron microprobe data for Tumanny Au-Ag-Hg compounds.

	1	2	3	4	5
Au	63.08	66.00	65.53	60.61	38.09
Ag	36.25	32.35	34.21	40.74	52.18
Hg	bdl	bdl	bdl	bdl	9.25
Total	99.33	98.35	99.74	101.35	99.52
Fineness	635	671	657	598	383

Samples: 994 (1), 758 (2–4), 769 (5).

(Kesler et al., 2003).

We also suggest that gabbroic dikes related to the first-phase gabbro of the Egdykgych Complex were the source for Ni and Co in arsenopyrite at Tumanny. This is consistent to a diorite intrusion origin for Ni-Co-bearing arsenopyrite with Ni and Co content up to 0.04 and 0.03 apfu, at the Freda Rebecca gold deposit (Klemm and Kraäutner, 2000). Ultramafic and mafic rocks were considered to be the source for Ni and Co in arsenopyrite from listvenite at the Haimur deposit, Egypt with up to 0.05 wt% Ni (Emam and Zoheir, 2013) and in Co-bearing arsenopyrite from altered lamprophyre dike in Krušné hory, Czech Republic (Pivec et al., 2002).

5.2. Whole-ore composition

Statistically significant and positive relationships between Pb-Ag-Cu-Zn-Cd-Zn (group 1), Au–As–Sb–Mo (group 2) and Au-Ag-Pb-Zn-Cu-As-Sb-Cd-Te-Se (group 3) reflect the mineralogical control in the element distribution.

The Pb-Ag-Cu-Zn-Cd-Zn association is related to carbonate-base metal assemblage, in which galena, sphalerite, and chalcopyrite are the major minerals. Positive correlations between elements within group 1 are testimony that these metals were predominantly deposited during the early base-metal stage. The strong relationship between Cd and Zn is consistent with substitution of Cd for Zn in sphalerite; the Cd content in early sphalerite is up to 0.5 wt%. In contrast, the strong relationship between Pb and Ag is not related to the presence of Ag in galena, because electron-microprobe analysis did not reveal any admixtures in this mineral except for Se. However, inclusions of Ag-bearing phases (hessite, Au-Ag alloys) belonging to the gold-silver-sulfosalt stage were found embedded in galena grains. This fact explains the strong relationship between Ag and Pb in group 1.

The Au–As–Sb–Mo association is related to the mineral assemblage formed at substage 1 of the gold-silver-sulfosalt stage and predominantly consisting of As-bearing pyrite III and arsenopyrite. As aforementioned Au-Ag alloy (electrum) at Tumanny is embedded in As-

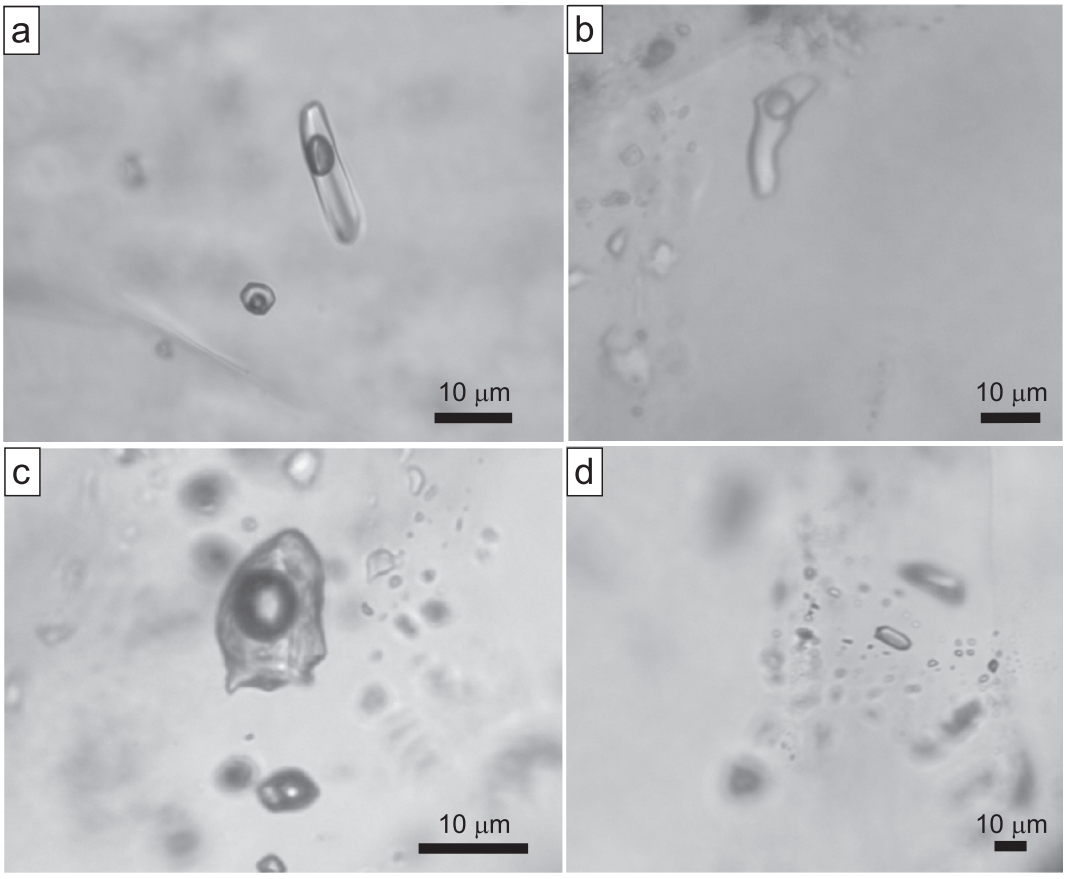

Fig. 11. Photomicrographs of primary fluid inclusions in quartz from the Tumanny prospect. (a-c) Two-phase inclusions of aqueous solution, (d) vapor inclusions.

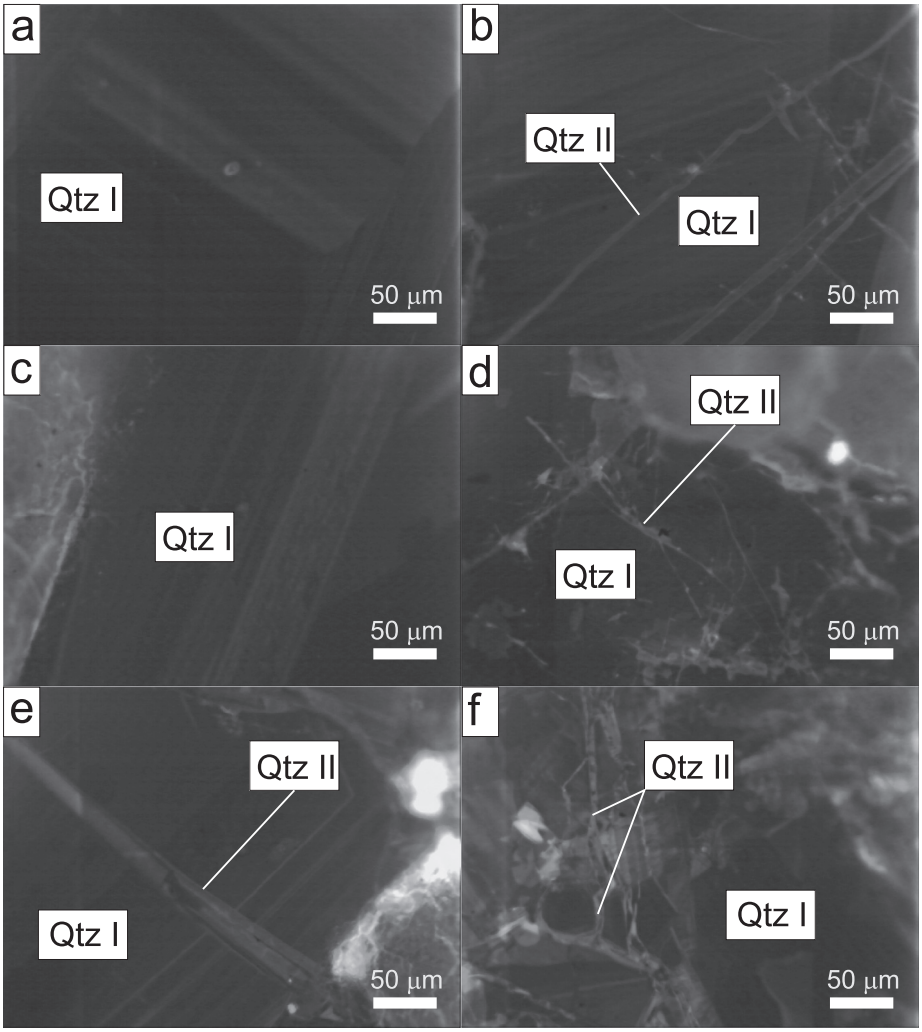

Fig. 12. CL images of quartz from the Tumanny prospect. (a, b) Quartz from veins containing carbonate-base metal assemblage, sample 759; (c, d) quartz from veins containing gold-silver-sulfosalt assemblage, sample 759; (e, f) quartz from veins containing overlapped assemblages, sample 1101.

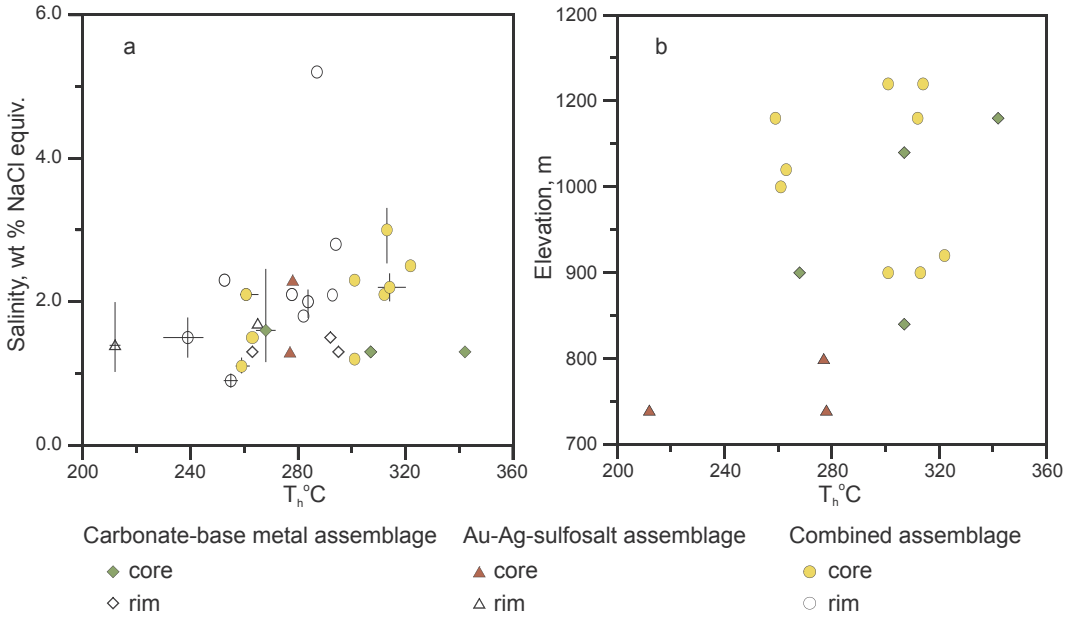

Fig. 13. Binary plots illustrating homogenization temperature of primary fluid inclusions, fluid salinities, and relationship between homogenization temperature and elevation at the Tumanny prospect. (a) T_h versus salinity plot, (b) T_h versus elevation plot.

Table 5
Microthermometric data for fluid inclusions in vein quartz of the Tumanny prospect.

Mineral assemblage	Number of sample	Elevation, m	FI type	Position of primary inclusions in crystal	Number of inclusions	T_{hom}. C	T_{eut}. C	$T_{ice\ melt}$, C	Salinity. wt% NaCl equiv.	D, g/cm^3
Carbonate-base metal	991	840	P*	core	3	307	−28	−0.8	1.3	0.69
			P*	rim	4	295	−28	−0.8	1.3	0.72
	760	900	P	core	24	266–273 (268)	−28 to −30	−0.7 to −1.5	1.2–2.5 (1.6)	0.77–0.78
			P*	rim	3	263	−25	−0.8	1.3	0.78
	956	1040	P*	core	6	307	−27	−0.8	1.3	0.69
			P*	rim	5	292	−29	−0.9	1.5	0.73
			S*		4	203	−27	−1.5	2.5	0.88
	771	1080	P*	core	3	342	−28	−0.8	1.3	0.61
			S*		3	232	−30	−0.9	1.5	0.84
Gold-silver-sulfosalt	757	740	P	rim	9	210–214 (212)	−30 to −31	−0.6 to −1.2	1.0–2.0 (1.4)	0.86–0.87
	758	740	P*	core	7	278	−32	−1.4	2.3	0.77
			P*	core	4	265	−32	−1.0	1.7	0.78
	759	800	P*	core	3	277	−30	−0.8	1.3	0.76
			S*		13	176	−30	−1.7	2.8	0.92
Overlapped	1011	900	P*	core	5	301	−28	−0.7	1.2	0.70
			P*	rim	3	282	−27	−1.1	1.8	0.75
			S		13	193–213 (207)	−28 to −29	−2.0 to −2.1	3.3–3.4 (3.4)	0.88–0.90
	1013	900	P*	core	2	313	−27	−1.8	3.0	0.71
			P*	rim	3	293	−28	−1.3	2.1	0.74
			S		7	163–185 (172)	−28 to −29	−1.5 to −1.6	2.5–2.6 (2.6)	0.90–0.93
	988	920	P*	core	15	322	−30	−1.5	2.5	0.68
			P*	rim	5	287	−30	−3.2	5.2	0.79
	767	1000	P	core	9	258–264 (261)	−30 to −31	−1.3	2.1	0.79–0.80
	994	1020	P*	core	4	263	−31	−0.9	1.5	0.78
	755	1080	P	core	8	257–262 (259)	−28to −30	−0.6 to −0.6	1.0–1.2 (1.1)	0.78–0.79
			P	rim	10	253–256 (255)	−26 to −29	−0.5	0.8–1.0 (0.9)	0.79–0.80
	756	1080	P	rim	7	230–245 (239)	−29 to −30	−0.7 to −1.0	1.2–1.7 (1.5)	0.82–0.83
	763	1080	P*	core	3	312	−27	−1.3	2.1	0.70
			P	rim	14	277–286 (284)	−28 to −29	−1.0 to −1.3	1.7–2.1 (2.0)	0.75–0.77
	970	1100	P*	rim	3	253	−29	−1.4	2.3	0.81
			S*		3	103	−26	−1.6	2.6	0.98
	769	1120	P	core	16	310–321 (314)	−24 to −31	−1.3 to −1.4	2.1–2.3 (2.2)	0.68–0.70
			P	rim	8	294–294 (294)	−28	−1.5 to −2.0	2.5–3.3 (2.8)	0.74–0.75
			S*		3	201	−29	−0.9	3.3	0.75
	770	1120	P*	core	7	301	−30	−1.4	2.3	0.72
			P*	rim	3	278	−30	−1.3	2.1	0.77

* One group of inclusions with identical homogenization temperature. (T_{hom}) Homogenization temperature, C; (T_{eut}) eutectic temperature, C; ($T_{ice\ melt}$) ice melting temperature, C; (D) density, g/cm^3. (P) Primary and (S) secondary inclusions. Average values are in parenthesizes.

bearing pyrite. In addition, gold as microinclusions may occur in As-bearing pyrite and arsenopyrite. The control of Au by arsenopyrite or As-rich pyrite has been previously documented (Hedenquist et al., 2000; Einaudi et al., 2003; John et al., 2003; Sung et al., 2009). Similar to group 1, positive relationship between Cd and Zn may reflect substitution Cd for Zn in sphalerite, however this relation is weaker.

This Au-Ag-Pb-Zn-Cu-As-Sb-Cd-Te-Se-Fe-S geochemical association is consistent with the overlapped assemblages consisting of minerals referred to the carbonate-base metal and gold-silver-sulfosalt assemblages. The high concentration of Ag, Au, Sb, and Te is consistent with a presence of phases typical of substage 2: hessite, Au-Ag alloys, Ttr_s, and polybasite. The strong relationship of Pb, Te, and Ag reflects the presence of hessite inclusions in galena. Intimate association of As and Sb is consistent with a presence of these elements in Ttr_s. The strong relationship of Fe and Zn in this assemblage is probably caused by Fe for Zn substitution in sphalerite (16 mol% FeS). Cu, Fe, Pb, As, and S can incorporate in the minerals belonging to both carbonate-base metal assemblage (chalcopyrite, galena) and early assemblage of gold-silver-sulfosalt stage.

Geochemical associations similar to those of groups 1 and 2 was previously described by Chinchilla et al. (2016) at the Patricia Zn–Pb–Ag IS epithermal deposit. Nikolaev et al. (2016) reported a geochemical assemblage like that of group 1 at the Vesenny Au-Ag IS epithermal prospect within the Baimka Cu-Mo-Au porphyry trend.

The Mo, Te, Bi and As anomalies in the prospect probably indicate magmatic contribution of metals in the mineralization similarly to that suggested for the epithermal prospects at the Milos Island, Greece (Alfieris and Voudouris 2005; Alfieris et al., 2013).

5.3. Fluid evolution and physicochemical conditions of mineralization

Fluid inclusion data show that quartz from the carbonate-base metal stage of the Tumanny prospect crystallized at temperature decreasing from 310 to 340 to 300–290 °C. CL-free crystal cores of this quartz were possibly formed from boiling fluid, whereas cathode luminescent oscillatory-zoned rims crystallized from homogeneous solution. Secondary inclusions in this quartz are homogenized at 200–230 °C. Quartz from gold-silver-sulfosalt stage also crystallized at temperature

Table 6
Average and maximal contents of metals and sulfur in quartz veins of the Tumanny prospect.

Element	Group 1 Geochemical assemblage **Pb** (AgCuZnCd)		Group 2 Geochemical assemblage **Au** (AsMoSb)		Group 3Geochemical assemblage **AuAgPb** (ZnCuAsSbCdTeSeFeS	
	Average (1) and maximal (2) contents					
	1	2	1	2	1	2
Au, ppm	0.12	0.37	3.1	37.6	1.0	9.5
Ag	14.6	49.6	14.4	60.7	91	908
As	54	618	387	9246	278	5770
Sb	14	54	65	246	113	1284
Pb	2142	11,600	313	922	3459	198,000
Zn	235	4239	37	764	303	9322
Cu	322	1863	49	504	345	18,500
Mo	7	105	39	125	24	154
Te	< 10	13	< 10	< 10	< 10	106
Se	< 10	40	< 10	< 10	< 10	53
Cd	1.2	27	< 0.5	2.4	1.6	49.4
Bi	< 2	11	< 2	3	< 2	23
Fe, %	0.96	1.5	1.26	4.32	1.85	16.3
S, %	0.14	0.47	0.15	1.83	0.47	4.97
Number of samples (fraction of total number of samples, %)	18 (16.2%)		15 (13.5%)		20 (18%)	

decreasing from 260 to 280 °C to ~210 °C (Fig. 13a). Crystal cores probably crystallized from boiling fluid, whereas rims crystallized from homogenous fluid. The homogenization temperature of primary inclusions in quartz rims is close to that of secondary inclusions in quartz from the carbonate base-metal stage. The substage I minerals of the gold-silver-sulfosalt stage possibly were formed at ~260 °C. It can be suggested that hessite, petzite, and electrum crystallized at ~210 °C. This suggestion is consistent with the geochemical studies at epithermal deposits. For example, So and Shelton (1987) showed that gold-silver deposition occurs at temperatures below 240 °C. Secondary inclusions in gold-silver-sulfosalt stage quartz homogenized approximately at 180 °C, which is consistent with imiterite formation (see above). Fluid inclusions in quartz from the veins containing both carbonate-base metal and gold-silver sulfosalt assemblages exhibit parameters characteristic of these both assemblages (Fig. 13a), indicating an overprint of gold-silver-sulfosalt stage on carbonate-base metal stage.

A homogenization temperature versus elevation plot (Fig. 13b) does not show any dependence between these parameters, reflecting an absence of vertical temperature zoning at the Tumanny prospect.

Mineralogical and fluid inclusion data allowed us to construct the evolution of mineralizing fluid at the Tumanny prospect (Fig. 15). This scheme shows decreasing log fS_2 sulfur from −8 at the formation of carbonate-base metal assemblage to −16 at the deposition of gold-silver-sulfosalt assemblage and attribution of the both studied mineral assemblages to the intermediate sulfidation type of epithermal mineralization.

6. Conclusions

This paper presents the first data on ore mineralogy and fluid inclusions for the Tumanny Au-Ag-Te-Hg prospect. Mineralization was formed during two stages carbonate-base metal and gold-silver sulfosalt, which contain similar minerals different in chemical composition. Pyrite is As-free and As-rich, respectively. Tennantite-tetrahedrite of the first stage is highly variable in the Sb/(Sb + As) ratio and has low Ag content, whereas the second stage tetrahedrite is weakly variable in the

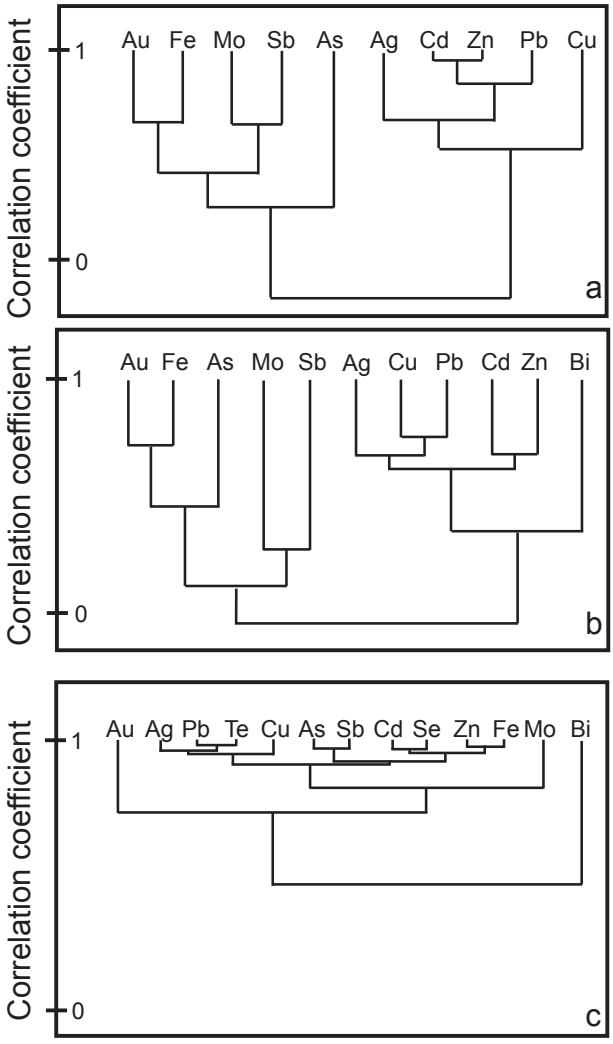

Fig. 14. Correlation dendrograms of elements within three groups of samples selected from quartz veins. (a) Group 1, geochemical association **Pb** (AgCuZnCd); (b) group 2, geochemical association **AuAgPb** (ZnCuAsSbCdTeSeFeS); (c) group 3, geochemical association **Au** (AsMoSb).

Sb/(Sb + As) and is enriched in Ag. Sphalerite from the both stages is different in the Fe content, 6 and 16 mol%, respectively. The major gold carrier is electrum with fineness 598–675. Silver is concentrated in electrum, hessite, polybasite, acanthite, and imiterite. Cluster analysis of the whole-ore geochemical data identified three geochemical associations two of which reflect the mineralization stages, whereas the third indicates overprint of them. Mineralogy of these assemblages controls the whole-ore composition. Fluid inclusion and CL studies revealed three generations of vein quartz crystallized at temperature decreased from 290 to 340 °C (carbonate-base metal stage), through 260–280 °C (substage I of gold-silver-sulfosalt stage) to 180–210 °C (substage II of gold-silver-sulfosalt stage). Salinities of fluids in primary inclusions and secondary inclusions from quartz I and II range from 0.8 to 5.2 wt% NaCl equiv. The ore mineralogy and composition of minerals, whole-ore geochemistry, and the temperature and salinity range of the fluids are consistent with the suggestion that the Tumanny prospect is an epithermal intermediate-sulfidation deposit.

Acknowledgments

We are grateful to V.Yu. Prokofiev for his assistance in fluid inclusion study and O.M. Zhilicheva for obtaining CL images. We thank reviewers Jeffrey Hedenquist and Panagiotis Voudouris and handling

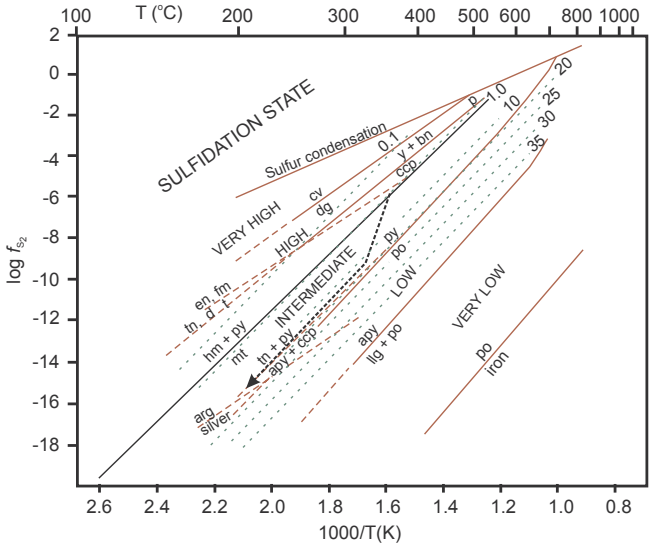

Fig. 15. fS_2-T diagram showing the variety of sulfide assemblages in epithermal deposits that reflects sulfidation state. Simplified from Einaudi et al. (2003) and Sillitoe and Hedenquist (2003). Arrow shows fluid evolution at Tumanny. Dash lines depict isopleths of FeS content (mol%) in sphalerite taken from Czamanske (1974). (cv) Covellite, (dg) digenite, (py) pyrite, (bn) bornite, (ccp) chalcopyrite, (en) enargite, (fm) famatinite, (tn) tennantite, (td) tetrahedrite, (hm) hematite, (mt) magnetite, (arg) argenthite, acanthite, (apy) arsenopyrite, (llg) löllingite, (po) pyrrhotite.5.

editor Olga Plotinskaya for their valuable comments, which significantly improved the manuscript.

References

Alfieris, D., Voudouris, P., 2005. Ore mineralogy of transitional submarine to subaerial magmatic-hydrothermal deposits in W. Milos, Greece. In: Cook, N., Bonev, I. (Eds.), Au-Ag-Te-Se deposits. Geochemistry, Mineralogy and Petrology, pp. 1–6 Sofia.

Alfieris, D., Voudouris, P., Spry, P.G., 2013. Shallow submarine epithermal Pb-Zn-Cu-Au-Ag-Te mineralization on western Milos Island, Aegean Volcanic Arc, Greece: Mineralogical, Geological and Geochemical constraints. Ore Geol. Rev. 53, 159–180.

Baksheev, I.A., Nikolaev, YuN., Prokof'ev, V.Yu, Marushchenko, L.I., Nagornaya, E.V., Chitalin, A.F., Sidorina, YuN., Kalko, I.A., 2014. Porphyry–epithermal copper- molybdenum-gold system of the Baimka trend, Western Chukchi Peninsula. In: Metallogeny of Ancient and Recent Oceans. XX Scientific School, Miass, April 2014. Institute of Mineralogy, Ural Branch, Russian Academy of Sciences, pp. 108–112 (in Russian).

Belyi, V.F., 1977. Stratigraphy and Structures of the Okhotsk-Chukotka Volcanic Belt. Nauka, Moscow (in Russian).

Bindi, L., Stanley, C.J., Spry, P.G., 2015. Cervelleite, Ag_4TeS: solution and description of crystal structure. Mineral. Petrol. 109, 413–419.

Bodnar, R.J., Vityk, M.O., 1994. Interpretation of microthermometric data for H_2O-NaCl fluid inclusions. In: de Vivo, B., Frezzotti, M.L. (Eds.), Fluid Inclusions in Minerals: Methods and Applications. IMA Short Course, pp. 117–130.

Brown, P., 1989. FLINCOR: a computer program for the reduction and investigation of fluid inclusion data. Am. Mineral. 74, 1390–1393.

Carrillo-Rosúa, J., Morales-Ruano, S., Morata, D., Boyce, A.J., Belmar, M., Fallick, A.E., Fenoll Hach-Alí, P., 2008. Mineralogy and geochemistry of El Dorado epithermal gold deposit, El Sauce district, central-northern Chile. Mineral. Petrol. 92, 341–360.

Chinchilla, D., Ortega, L., Piña, R., Merinero, R., Moncada, D., Bodnar, R.J., Quesada, C., Valverde, A., Lunar, R., 2016. The Patricia Zn–Pb–Ag epithermal ore deposit: An uncommon type of mineralization in northeastern Chile. Ore Geol. Rev. 73, 104–126.

Criddle, A.J., Chisholm, J.E., Stanley, C.J., 1989. Cervelleite, Ag_4TeS, a new mineral from the Bambolla mine, Mexico, and a description of a photo-chemical reaction involving cervelleite, acanthite and hessite. Eur. J. Mineral. 1, 371–380.

Crawford, M.L., 1981. Phase equilibria in aqueous fluid inclusions. In: Hollister, L.S., Crawford, M.L. (Eds.), Fluid Inclusions: Applications to Petrology. Mineralogical Association of Canada Short Course Handbook, pp. 75–100.

Czamanske, G.K., 1974. The FeS content of sphalerite along the chalcopyrite-pyrite-bornite sulfur fugacity buffer. Econ. Geol. 69, 1328–1334.

Emam, A., Zoheir, B., 2013. Au and Cr mobilization through metasomatism: microchemical evidence from ore-bearing listvenite, South Eastern Desert of Egypt. J. Geochem. Explor. 125, 34–45.

Einaudi, M.T., Hedenquist, J.W., Inan, E.E., 2003. Sulfidation state of fluids in active and extinct hydrothermal systems: Transition from porphyry to epithermal environments. In Volcanic, geothermal and ore-forming fluids: Rulers and witnesses of processes within the Earth. Society of Economic Geologists, pp. 285–313 Special Publication 10.

Fadda, S., Fiori, M., Grillo, S.M., 2005. Chemical variations in tetrahedrite -tennantite minerals from the Furtei epithermal Au deposit, Sardinia, Italy: Mineral zoning and ore fluids evolution. Geokhim. Mineral. Petrol. 43, 80–84.

Filatova, N.I., 1988. Peri-oceanic volcanic belts. Nedra, Moscow (in Russian).

Guillou, J.-J., Monthel, J., Picot, P., Pillard, F., Protas, J., Samama, J.-C., 1985. L'imitérite, Ag_2HgS_2, nouvelle espece minérale propriétés et structure crystalline. Bull. Minéral. 108, 457–464.

Hourigan, J.K., Akinin, V.V., 2004. Tectonic and chronostratigraphic implications of new $^{40}Ar/^{39}Ar$geochronology and geochemistry of the Arman and Maltan-Ola volcanic fields, Okhotsk-Chukotka volcanic belt, Northeastern Russia. Geol. Soc. Am. Bull. 116, 637–654.

Hedenquist, J.W., Arribas Jr., A., Urien-González, E., 2000. Exploration for epithermal gold deposits. Rev. Econ. Geol. 13, 245–277.

Ispolatov, V.O., Tikhomirov, P.L., Heizler, M., Cherepanova, I.Yu., 2004. New $^{40}Ar/^{39}Ar$ ages of Cretaceous continental volcanics from Central Chukotka: Implications for initiation and duration of volcanism within the northern part of the Okhotsk-Chukotka volcanic belt (Northeastern Eurasia). J. Geol. 112, 369–377.

John, D.A., Hofstra, A.H., Fleck, R.J., Brummer, J.E., Saderholm, E.C., 2003. Geologic setting and genesis of the Mule Canyon low-sulfidation epithermal gold-silver deposit, north-central Nevada. Econ. Geol. 98, 425–463.

Kesler, S.E., Russel, N., McCurdy, K., 2003. Trace elements content of the Pueblo Viejo precious-metal deposits and their relation tom other high-sulfidation epithermal systems. Mineral. Deposita. 38, 668–682.

Klemm, D.D., Kraäutner, H.G., 2000. Hydrothermal alteration and associated mineralization in the Freda-Rebecca gold deposit, Bindura District, Zimbabwe. Minerl. Deposita 35, 90–108.

Kotova, M.S., Nagornaya, E.V., Anosova, M.O., Kostitsyn, YuA., Baksheev, I.A., Nikolaev, YuN., Kalko, I.A., 2012. Dating of wall-rock alteration process and ore-bearing granitoids of the Nakhodka ore field, Western Chukchi Peninsula. In: Geochronological Isotopic Systems, Methods of Their Study, and Chronology of Geological Processes, V Russian Isotope Conference in Geochronology, Moscow, June, 2012. Institute of Geochemistry and Analytical Chemistry, pp. 181–184 (in Russian).

Kovalenker, V.A., Tsonev, D., Breskovska, V.V., Malov, V.C., Troneva, N.V., 1986. New data on the mineralogy of copper-sulphide deposits Mittelgebirge Central Bulgaria. In: Korzhinsky, D.S. (Ed.), Metasomatism, Mineralogy and Problems of Genesis of Gold and Silver Deposits in the Volcanic Sequences. Nauka, Moscow, pp. 91–110 (in Russian).

Kuzhuget, R.V., Zaikov, V.V., Lebedev, V.I., Mongush, A.A., 2015. Gold mineralization of the Khaak-Sair gold-quartz ore occurrence in listwanites (western Tuva). Russ. Geol. Geophys. 56, 1332–1348.

Levresse, G., Bouabdellah, M., Cheilletz, A., Gasquet, D., Maacha, L., Tritlla, J., Banks, D., Rachid, A.S.M., 2016. Degassing as the main ore-forming process at the giant Imiter Ag–Hg vein deposit in the Anti-Atlas Mountains, Morocco. In: Bouabdellah, M., Slack, J.F. (Eds.), Mineral Deposits of North Africa. Mineral Resource Reviews, pp. 85–106.

Marushchenko, L.I., Baksheev, I.A., Nagornaya, E.V., Chitalin, A.F., Nikolaev, YuN., Vlasov, E.A., 2017. Compositional evolution of the tetrahedrite solid solution in porphyry-epithermal system: A case study of the Baimka Cu-Mo-Au trend, Chukchi Peninsula, Russia. Ore Geol. Rev http://dx.doi.org/10.1016 j.oregeorev.2017.01.018.

Moll-Stalcup, E.J., Lane, L.S., Cecile, M.P., Gorodinsky, M.E., 1995. Geochemistry and U-Pb geochronology of arc-related magmatic rocks, Northeastern Russia. In: Geol Soc Amer 91st Annual Cordilleran Section. Univ Alaska, Fairbanks, pp. 65.

Nikolaev, Yu.N., Baksheev, I.A., Prokofiev, V.Yu., Nagornaya, E.V., Marushchenko, L.I., Sidorina, Yu.N., Chitalin, A.F., Kal'ko, I.A., 2016. Gold–silver mineralization in porphyry–epithermal systems of the Baimka trend, Western Chukchi Peninsula, Russia. Geol. Ore Deposits 58, 319–345.

Pivec, E., Holub, F.V., Lang, M., Novák, J.K., Štemprok, M., 2002. Rock-forming minerals of lamprophyres and associated mafic dykes from the Krušné hory/Erzgebirge (Czech Republic). J. Czech. Geol. Soc. 47 (12), 23–32.

Sillitoe, R.H., Hedenquist, J.W., 2003. Linkages between volcanotectonic settings, ore-fluid compositions, and epithermal precious metal deposits. Econ. Geol. Spec. Publ. 10, 315–343.

Plotinskaya, O.Y., Grabezhev, A.I., Groznova, E.O., Seltmann, R., Lehmann, B., 2014. The Late Paleozoic porphyry–epithermal spectrum of the Birgilda-Tomino ore cluster in the South Urals, Russia. J. Asian Earth Sci. 79B, 910–931.

So, C.S., Shelton, K.L., 1987. Stable isotope and fluid inclusion studies of gold- and silver-bearing hydrothermal vein deposits. Cheonan-Cheongyang mining district, Republic of Korea: Cheonan area. Econ. Geol. 82, 987–1000.

Spiridonov, E.M., Filimonov, S.V., Kulikova, I.M., Nazmova, G.N., Krivitskaya, N.N., Bryzgalov, I.A., Korotaeva, N.N., 2008. Minerals of the fahlore group as indicators of ore formation. In: Problems of geology of ore deposits, mineralogy, petrology, and geochemistry. IGEM RAS, Moscow, pp. 356–359 (in Russian).

Sung, Y.H., Brugger, J., Ciobanu, C.L., Pring, A., Skinner, W., Nugus, M., 2009. Invisible gold in arsenian pyrite and arsenopyrite from a multistage Archaean gold deposit: Sunrise Dam, Eastern Goldfields Province, Western Australia. Miner. Deposita 44, 765–791.

Tikhomirov, P.L., Prokofiev, V.Yu, Kal'ko, I.A., Apletalin, A.V., Nikolaev, YuN., Kobayashi, K., Nakamura, E., 2017. Post-collisional magmatism of western Chukotka and Early Cretaceous tectonic rearrangement in northeastern Asia. Geotectonics 51 (2), 131–151.

Vorobiov, S.A., 2000. The Gold-Digger Software Package for Complex Processing of Geological and Geochemical Data. Documentation and Description. Ministry of Natural Resources of Russian Federation, Moscow (in Russian).

Voudouris, P., 2011. Conditions of formation of the Mavrokoryfi high-sulfidation

epithermal Cu-Ag-Au-Te deposit (Petrota Graben, NE Greece). Mineralogy and Petrology 101, 97–113.
Voudouris, P., Melfos, V., Spry, P.G., Kartal, T., Schleicher, H., Moritz, R., Ortelli, M., 2013. The Pagoni Rachi/Kirki Cu-Mo-Re-Au-Ag-Te deposit, northern Greece: mineralogical and fluid inclusion constraints on the evolution of a telescoped porphyry-epithermal system. The Canadian Mineralogist 51, 411–442.
Voudouris, P., Spry, P.G., Sakellaris, G.A., Mavrogonatos, C., 2011. A cervelleite-like mineral and other Ag-Cu-Te-S minerals [Ag_2CuTeS and $(Ag, Cu)_2TeS$] in gold-bearing veins in metamorphic rocks of the Cycladic Blueschist Unit, Kallianou, Evia Island, Greece. Mineralogy and Petrology 101, 169–183.
Voudouris, P., Tarkian, M., Arikas, K., 2006. Mineralogy of telluride-bearing epithermal ores in Kassiteres-Sappes area, western Thrace, Greece. Mineral. Petrol. 87, 31–52.